DE GRUYTER DOI 10.1515/aot-2013-0063 — Adv. Opt. Techn. 2014; 3(1): 65–90

Review Article

Xinbin Cheng and Zhanshan Wang*

Defect-related properties of optical coatings

Abstract: Defects in optical coatings are a major factor degrading their performance. Based on the nature of defects, we classified them into two categories: visible defects and non-visible defects. Visible defects result from the replication of substrate imperfections or particulates within the coatings by subsequent layers and can increase scattering loss, produce critical errors in extreme ultraviolet lithography, weaken mechanical and environmental stability, and reduce laser damage resistance. Non-visible defects mainly involve a decrease in laser damage resistance but typically have no influence on other properties of optical coatings. In the case of widely used HfO_2/SiO_2 dielectric coatings, metallic Hf nano-clusters, off-stoichiometric HfO_2 nano-clusters, or areas of high-density electronic defects have been postulated as possible sources for non-visible defects. The emphasis of this review is devoted to discussing localized defect-driven laser-induced damage (LID) in optical coatings used for nanosecond-scale pulsed laser applications, but consideration is also given to other properties of optical coatings such as scattering, environmental stability, etc. The low densities and diverse properties of defects make the systematic study of LID initiating from localized defects time-consuming and very challenging. Experimental and theoretical studies of localized defect-driven LID using artificial defects whose properties can be well controlled are highlighted.

Keywords: artificial defects; defect-induced modification; laser-induced damage; optical coatings.

OCIS Classification Codes: 310.0310; 140.3330; 290.0290; 340.7470.

***Corresponding author: Zhanshan Wang,** MOE Key Laboratory of Advanced Micro-Structured Materials, Shanghai, 200092, China; and Institute of Precision Optical Engineering, School of Physics Science and Engineering, Tongji University, Shanghai, 200092, China, e-mail: wangzs@tongji.edu.cn
Xinbin Cheng: MOE Key Laboratory of Advanced Micro-Structured Materials, Shanghai, 200092, China; and Institute of Precision Optical Engineering, School of Physics Science and Engineering, Tongji University, Shanghai, 200092, China

www.degruyter.com/aot
© 2014 THOSS Media and De Gruyter

1 Introduction

Optical coatings are enabling technology for the development of modern optical systems. The final performance of an optical system is highly correlated with the performance of optical coatings. Unfortunately, defects, that are unavoidable in real-world optical coatings, sometimes lead to critical performance degradation. With the ever-increasing requirement to improve the sensitivity of high-precision applications such as ring-laser gyroscopes [1] and gravitational-wave detectors [2], etc., the total loss of optical coatings has been pushed to the level of parts per million (ppm). A few localized defects in optical coatings can substantially increase the scattering loss to tens or hundreds of ppm [3]. Extreme ultraviolet (EUV) lithography has also introduced a new challenge for defect control [4]. Due to the very short wavelength, defects with diameters of a few nanometers in the Mo/Si multilayer can disturb the phase of light reflected from a mask, thereby producing critical errors in the lithographic image of the mask pattern. In practice, optical coatings are frequently used in hygrothermal and even harsher environments. Defects open the channels for moisture or contaminant to diffuse into the coatings and generate localized high stress, which reduces the environmental stability of optical coatings and causes mechanical failure [5]. It has also been well recognized that LID in optical coatings is driven by localized defects. It is probably fair to say that most studies exploring the defect-related properties of optical coatings are devoted to investigating the influence of defects on laser damage resistance of optical coatings. Following the construction of fusion-scale lasers such as the National Ignition Facility [6], Laser Megajoule [7], Shenguang [8], etc., research on LID in optical components becomes more and more extensive and intensive. The aim of this review is to summarize important findings on defect-related properties of optical coatings with a strong emphasis on localized defect-driven LID.

According to their nature, defects in optical coatings are categorized into two types: visible defects and non-visible defects. For visible defects, their origin and growth in coatings are first discussed. Then the influence of visible defects on the performance of coatings is

discussed. Consideration is also given to the solutions to reduce visible defects. For non-visible defects, attention is mainly devoted to LID initiating from nano-absorbing defects.

There are some points that should be noted in the following sections in relation to LID in optical coatings. We placed an emphasis on LID in optical coatings irradiated by nanosecond-pulsed laser from near ultraviolet (UV) to near infrared (IR) regions. There are two reasons for this decision. One is that these coatings are widely used in fusion-scale lasers and are the most extensively studied. Another is that localized defects play a more dominant role in LID of optical coatings at the nanosecond regime rather than at the picosecond and femtosecond regimes. In a further attempt to narrow the scope of this review, only HfO_2, Ta_2O_5, and SiO_2 dielectric coatings are considered. More importantly, we focus on LID studies using artificial defects, because artificial defects whose properties are well known and controlled promote reliable and efficient experimental studies and enable meaningful comparisons with simulation results.

2 Visible defects

2.1 Origin and growth of visible defects

2.1.1 Nodular defects

Nodular defects grow from particulates or seeds into an inverted conical shape with a domed top protruding above the surface of the coatings. Nodules have been observed in optical coatings prepared by different deposition technologies, such as thermal evaporation [9], electron beam evaporation (EBE) [10], magnetron sputtering [11], ion beam sputtering [12], chemical vapor deposition [13], plasma polymerization [14], etc. It is fair to say that nodules are the most extensively studied defects in optical coatings. Focused ion beam (FIB) technology has been widely used to cross-section nodules to expose the depth, composition, and shape of seeds. The origin of seeds has been well documented and is classified into two categories. Seeds could either be on the substrate surface due to insufficient cleaning, recontamination during handling, pumping, electron gun warming up, or presputtering processes, etc., or they could also be within the coatings because the evaporation or sputtering source can produce particulates by several mechanisms including arcing, electrostatic repulsion, gas explosions, temperature-induced solid-state phase, etc.

A collection of cross-sectional scanning electron microscope (SEM) micrographs showing different origins of seeds is given in Figure 1. In Figure 1A–C, the coatings are HfO_2/SiO_2 multilayers that were prepared by the EBE process. In Figure 1D, the coating is a Ta_2O_5/SiO_2 multilayer prepared by a magnetron sputtering process. The light layers are high-index materials of HfO_2 or Ta_2O_5, and the dark layers are SiO_2. By comparing the seed contrast with the contrast of the deposited materials, the composition of the seed can be inferred. Figure 1A gives the morphology of a nodule that was created from a seed on the substrate [15]. The seed could be organic material whose index is close to SiO_2. The nodule in Figure 1B originated from dark seeds that might result from the splattering of the SiO_2 evaporation source [12]. Figure 1C shows that the nodule was created from a light seed that was ejected from the HfO_2 evaporation source [16]. The nodule in Figure 1D originated from an elongated SiO_2 seed, the cause of which might be electrostatic repulsion of charged particles from the sputtering target or shutter. The defect in Figure 1D does not resemble a classic nodular geometry [11], and this type of defect is sometimes called a spatter defect.

Here we limit the discussion of nodular growth to the most widely studied case: films deposited on rotating

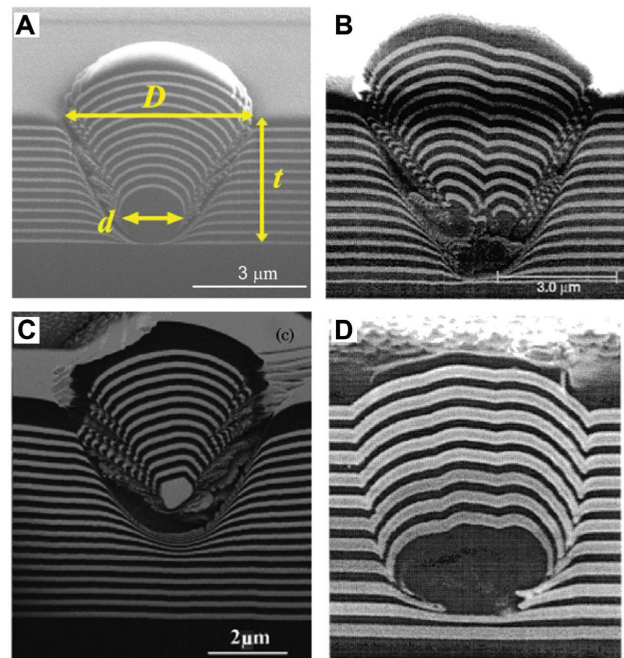

Figure 1 Cross-sectional SEM images of different nodules to show their origins. (A) From a seed on substrate surface [15], (B) from an SiO_2 seed within the multilayer (reproduced from Stolz et al. [12]), (C) from a HfO_2 seed within the multilayer (reproduced from Liu et al. [16]), and (D) from an elongated SiO_2 seed within the multilayer (reproduced from Stolz et al. [12]).

substrates by the EBE process. The growth behavior of nodules has a direct influence on their geometric characteristics and boundary structure. A simple model has been proposed to represent the geometries of classic nodules initiating from spherical seeds, where the nodular diameter, *D*, is related to a constant, *C*, to the seed diameter, *d*, and to the seed depth, *t*, via the relation *D*=sqrt(*Cdt*) [11], as shown in Figure 1A. The coefficient, *C*, indicates how bigger a nodule will grow compared with the seed. Due to a self-shadowing effect of the seed and to the insufficient mobility of evaporated atoms, discontinuous boundaries between the nodule and the surrounding thin films usually exist with many voids, which affect the mechanical stability of the nodule.

Here the influence of seed diameter and deposition condition on nodular growth is demonstrated by investigating artificial nodules that grow from silica microspheres on substrates. Figure 2 shows the cross-sectional patterns of nodules initiating from artificial silica microspheres with diameters of 0.6, 0.9, and 1.9 μm [17]. HfO_2/SiO_2 high-reflection (HR) coating in Figure 2A–C was prepared by the EBE process. These nodules possess an aspect ratio of *D*=sqrt(4*dt*). Seeds having a larger diameter shadow the incoming evaporation flux more effectively and cause more voids, which results in more discontinuous boundaries between nodule and surrounding film. Moreover, shadowing effects become weaker as the film grows. The boundaries gradually heal and become more continuous compared with the boundaries near the seeds. HfO_2/SiO_2 HR coating in Figure 2D–F was prepared by the ion-assisted deposition (IAD) process. Because the mobility of evaporated atoms is greatly enhanced by ion bombardment, these nodules possess a smaller aspect ratio of *D*=sqrt(2.5*dt*). This observation is in accordance with the simulation results that a smaller nodular diameter would result from either a higher mobility of deposited atoms or a smaller incident angle of evaporated atoms [18]. Moreover, the boundary continuity between the nodules and surrounding films is also significantly improved by increasing the mobility of deposited atoms. For a nodule initiating from a 1.9 μm seed, the discontinuous boundaries heal much faster and are close to being continuous after the growth of the whole stack. More continuous boundaries lead to stronger mechanical and environment stability.

2.1.2 Defects originating from substrate imperfections

When a brittle material, such as glass, is ground and polished, irreversible deformation can occur if the critical

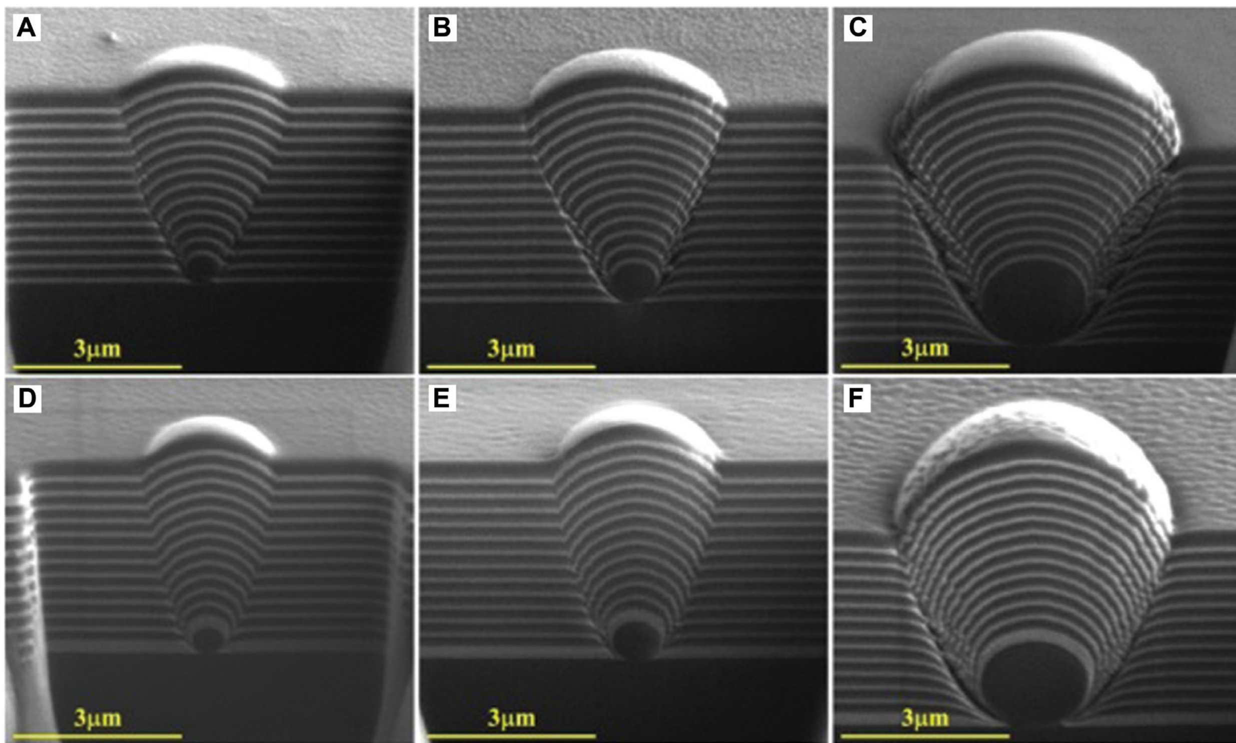

Figure 2 Cross-sectional SEM images of different nodules that grow from artificial silica microspheres; EBE process: (A) 0.6 μm, (B) 0.9 μm, (C) 1.9 μm; IAD process: (D) 0.6 μm, (E) 0.9 μm, (F) 1.9 μm [17].

resolved shear stress exceeds the elastic yield stress. All surfaces of machined glass substrates are imperfect to some extent. Scratches and digs are commonly identified as surface irregularities. The US Military Surface Quality Specification, MIL-PRF-13830, has been the most widely adopted standard to specify surface imperfections. Two numbers are always specified, for example, 40–20; the first number specifies the maximum width of scratches on the surface in tenths of a micron, and the second number defines the average maximum diameter of a dig in hundredths of a millimeter. Implied specifications of MIL-PRF-13830 also count the sum of smaller scratches and digs. Usually, 10–5 represents a precise standard for very demanding high power laser applications. However, scratches are more usually classified according to their morphologies rather than dimensions to predict their laser damage resistance. Figure 3 shows three categories of scratches that were prepared and observed by Suratwala et al [19]. Plastic scratches appear smooth and shallow without showing any irregularity along their path, and are often referred to as sleeks. Brittle scratches appear jagged and nearly discontinuous, with small lateral cracks. Mixed scratches contain both plastics modification and cracks. Brittle-type scratches can induce sub-band gap absorption and significantly reduce the LID damage threshold of uncoated optics, whereas plastic-type scratches are usually benign.

Scratches and digs affect the nucleation of deposited atoms and the formation of subsequent layers. The growing layers will replicate the defective features to some degree, causing the defects to propagate towards the surface of coatings. Two examples that were prepared by the sputtering and EBE processes are presented here to show the influence of these defective features on the morphology of multilayer coatings. Figure 4 presents transmission electron microscope (TEM) micrographs showing cross-sectional views of a reflective multilayer consisting of 50 bilayers of Mo and Si on substrates with tiny scratches [20]. When using a smoothing deposition technique, the topography of the scratch expands towards the top of a multilayer from 20 nm wide to 60 nm wide, but the depth of the defect becomes shallower as the film grows thicker, as shown in Figure 4A. If a non-smoothing deposition technique is used, the defect topography is more or less preserved throughout the multilayer, as shown in Figure 4B. Another example is provided to show that the alteration of the layer topography can be more significant if the scratches have bigger and more complicated structures. Figure 5A is an SEM image showing a cross-sectional view of a HR coating of 24 alternating HfO_2 and SiO_2 layers deposited on a substrate with trailing indent scratches [21]. The growing layers follow the morphology of the highly deformed trench and lose their planar nature. Figure 5B is a cross-sectional view of a 1 μm wide substrate sleek overcoated with HR coating. The coating can self-heal over the first several layers and completely recover its flatness during the coating growth. Figure 5C shows the morphology of the multilayer coating deposited on a wider sleek with three ripples. Although the resulting coating demonstrates a self-healing nature, it does

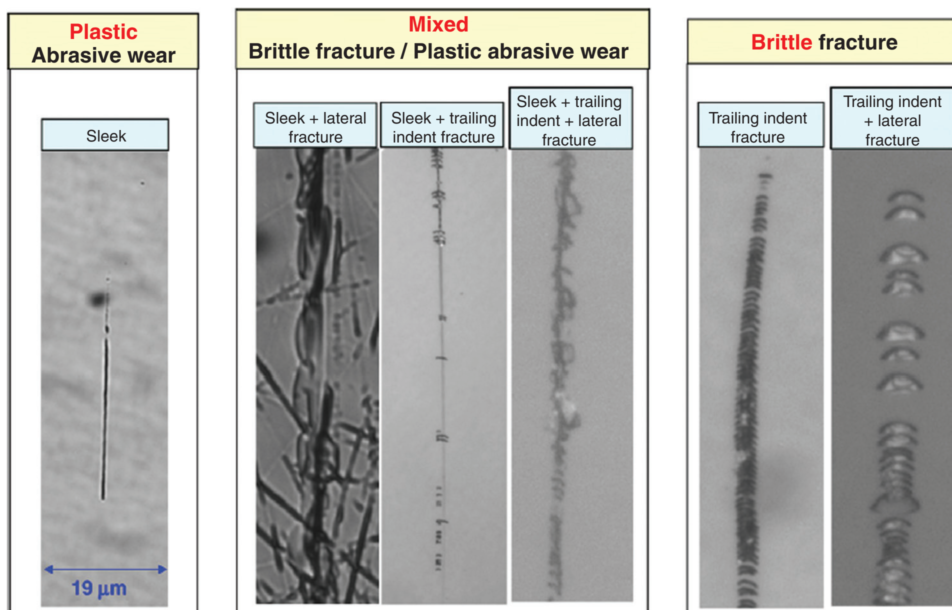

Figure 3 Categories of different types of scratches observed in samples (reproduced from Suratwala et al. [19]).

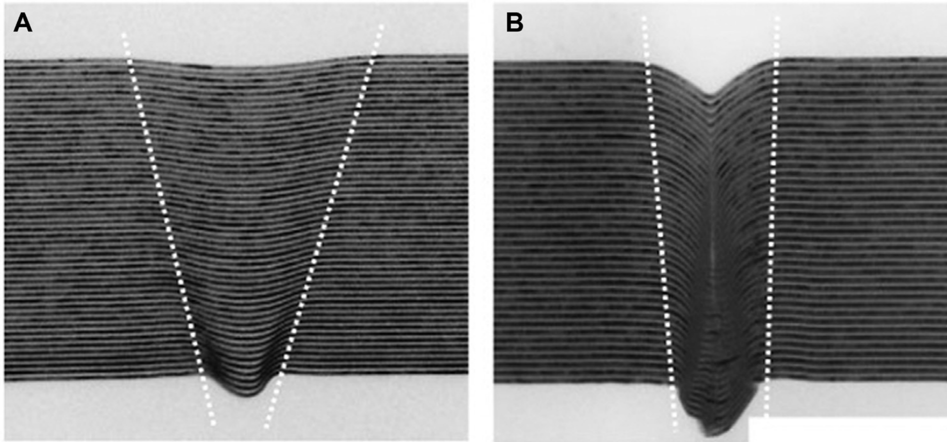

Figure 4 Cross-sectional TEM images of Mo/Si multilayers deposited on substrate scratches. The dotted white lines show how much the topography of a defect expands laterally from the bottom to the top of the coatings: (A) on a 20 nm wide scratch with smoothing deposition, (B) on a 40 nm wide scratch with non-smoothing deposition (reproduced from Sugawara et al. [20]).

not completely achieve planarity, thus forming a dome on the top layer. The above results demonstrate that the morphology of the resulting defect is affected not only by the morphology of substrate imperfections but also deposition conditions. The influence of these defects on the properties of optical coatings will be discussed in detail in the following sections.

2.2 The influence of defects on LID of optical coatings

2.2.1 Nodular defects

For HR coatings and polarizers working in the near IR region, nodules are the most problematic defects that

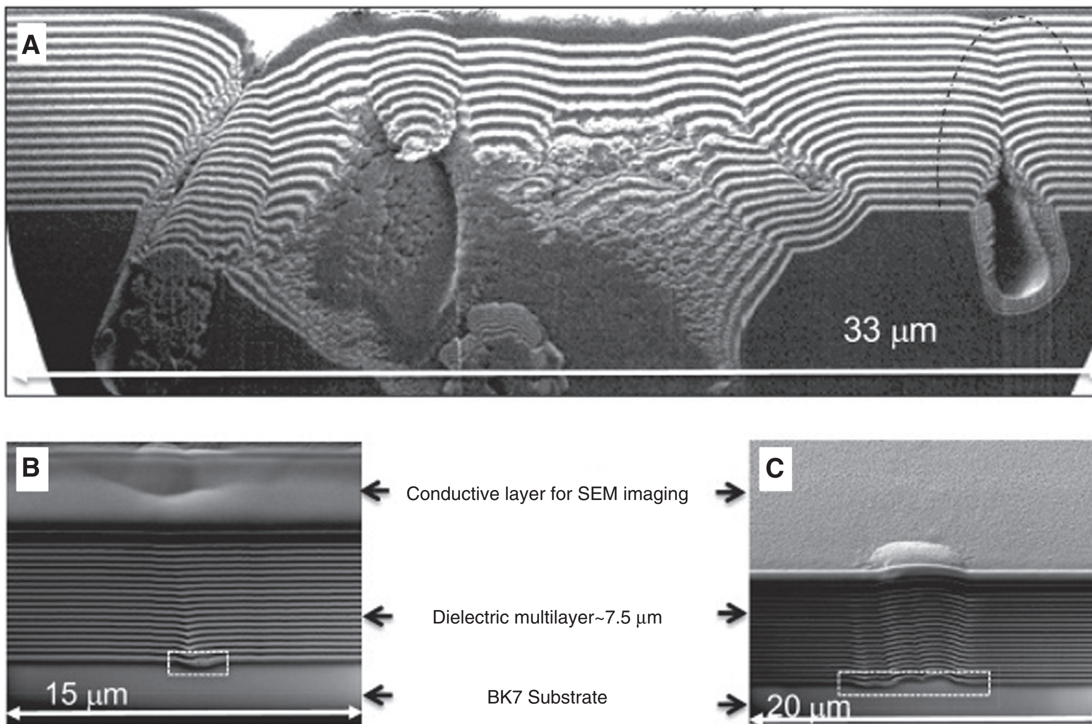

Figure 5 Cross-sectional SEM images of a HfO_2/SiO_2 HR coating deposited on substrate scratches: (A) on an etched trailing indent type scratch, (B) on an unetched, sleek type scratch, and (C) on an etched sleek type scratch (reproduced from Qiu et al. [21]).

decrease the laser-induced damage threshold (LIDT). Previous works on nodule-driven LID in optical coatings will be reviewed from four aspects: experimental studies, mechanical stability, electric-field (E-field) enhancement, and solutions to eliminate seeds or to lower the impact of existing seeds.

2.2.1.1 Experimental studies of nodular damage

Groups from the Lawrence Livermore National Laboratory have carried out pioneering work on determining which types of nodules are the most susceptible to LID. They developed statistics on the heights and diameters of nodules in HfO_2/SiO_2 HR coatings and found that defects with heights larger than 0.6 μm were most susceptible to LID [22]. Subsequent research from the Kaiser group showed that nodular defects with heights >1 μm rather than 0.6 μm were vulnerable to LID [23]. Such a discrepancy between the critical heights of nodules in different HfO_2/SiO_2 HR coatings is very usual, because the composition and lodging depth of seeds can be very different for coatings prepared by different vendors, and these factors have a huge influence on the damage resistance of nodules.

For real nodules, the seed density is usually very low and the diameter, absorption, and lodging depth of seeds are very difficult to predict, control, or reproduce. This complex situation makes the systematic and quantitative study of nodular damage very difficult. Creating nodules from artificial seeds whose properties can be well controlled offers the possibility of studying the LID of nodules in a more reliable and efficient way. Poulingue et al. have used diamond and silica seeds on the substrate surface to create artificial nodules [24]. The damage testing results showed that the nodule size was the critical parameter for the damage threshold, whereas nodular density was not critical. They also found that the critical seed size was between 0.5 and 1 μm, which is in good agreement with previous conclusions. Wei et al. investigated the damage behaviors of artificial nodules that were created from much smaller gold and SiO_2 nanoparticles [25]. A qualitative conclusion that both the composition and size influenced the structure and the LIDT of nodular defects was obtained.

Recently, we have created artificial nodules from monodisperse seeds and studied their damage characteristics [17], where the seed diameters, seed absorption, and film absorption were varied independently to evaluate their influence on the LIDTs of nodules. Figure 6 shows the statistical ejection fluences of artificial nodules. LIDTs of nodules monotonically decrease with increasing diameter of silica microspheres. Compared with the EBE process, the IAD process actually improved the boundary continuity but increased the film absorption. The 40 ppm absorption of IAD films was too high, which decreased the ejection fluences of nodules significantly. Absorbing seeds also significantly decreased the laser damage resistance of nodules. The above orthogonal experiments showed that there are many factors affecting the laser damage resistance of nodules apart from seed diameter and nodular height. It is impractical to predict the laser damage resistance of nodules without knowing their properties in detail. Taking 60 J/cm² (10 ns) as a required fluence (functional damage is not considered here), the control of seed diameter for different deposition processes and different seed absorptivity was very different. For HR coatings prepared by the EBE process, non-absorbing seeds whose diameter is larger than 1.4 μm should be removed to meet the required fluence, whereas absorbing seeds whose diameter is larger than 0.5 μm must be removed to obtain an LIDT higher than 60 J/cm². For HR coatings prepared by the IAD process, non-absorbing seeds whose diameter is larger than 0.9 μm must be removed to meet the required fluence. Such orthogonal experiments also provide valuable information for the optimization of cleaning and deposition processes. The damage behaviors of nodules initiating from seeds of different sizes and absorptivity can basically be explained from the aspects of boundary imperfection and E-field intensification. The following sections detail the damage mechanisms of nodules.

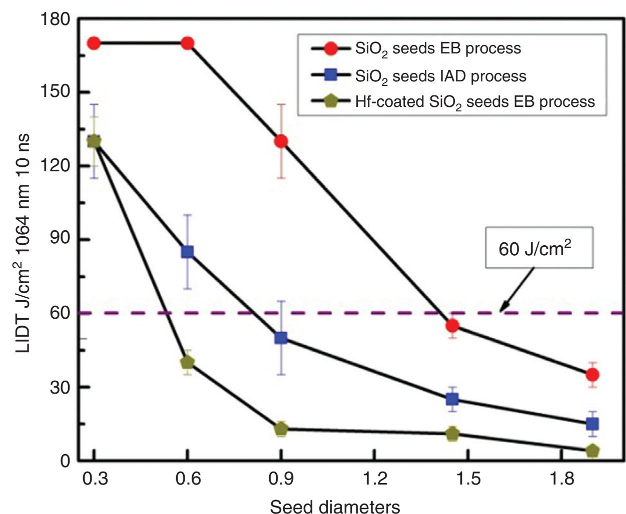

Figure 6 Statistical ejection fluences of artificial nodules that were prepared by EBE and IAD processes; the seeds were monodisperse silica microspheres and Hf-coated silica microspheres.

2.2.1.2 Understanding nodular damage from the aspect of mechanical stability

A general description of the thermomechanical damage of nodules irradiated by a nanosecond pulse laser is given as follows [26]. The nodules are first heated after absorbing the intensified light in the nodules. The discontinuous boundary between the nodules and the surrounding coatings restricts heat flow and increases the temperature gradient, developing stresses between the hot nodules and the colder surrounding films. When this stress reaches a critical value, the mechanically unstable nodules are ejected. Both light intensification (or E-field enhancement) in nodules and mechanical instability contribute to nodular damage. Here the mechanical behavior of nodules is first discussed. Poulingue et al. designed an experiment to analyze the damage initiating from nodules through a purely mechanical approach [27]. The artificial nodules were obtained by dispersing diamond particles on polished aluminum substrates before the deposition of the layers. Mechanical damage was progressively induced by pulling the samples in tension in an SEM. *In situ* observation showed that bigger nodular defects opened cracks at lower strains. One illustration is given in Figure 7. It was observed that nodular defects with a mean diameter larger than 4 μm are always associated with cracks. This result is in fairly good agreement with their laser damage test result that nodular defects with a diameter above 4 μm were frequently ejected. This is an ingenious approach showing that nodules are mechanically weak and the LID of nodules can be at least partially explained by a fracture-based model.

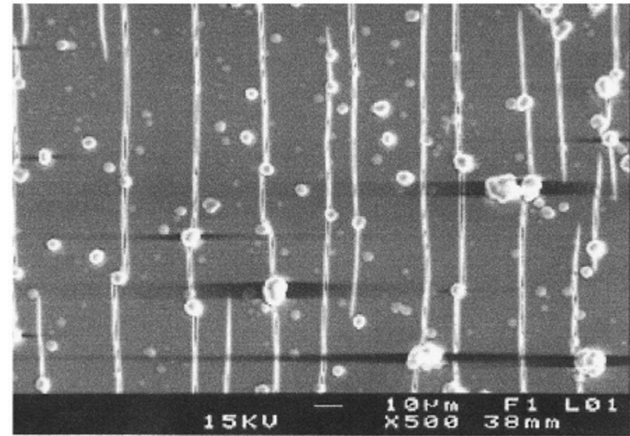

Figure 7 SEM micrograph showing the crack opening from nodular defects initiating from diamond seeds (reproduced from Poulingue et al. [27]).

2.2.1.3 Understanding of nodular damage from the aspect of E-field enhancement

The E-field intensity ($|E|^2$) distribution determines the spatial distribution of the absorbed laser energy in the area surrounding a nodule, knowledge of which is an important precondition to understanding the subsequent complex processes of temperature distribution, stress response, and mechanical damage. With the exception of the thermomechanical effect, the interaction between the intense field and the materials, via linear and nonlinear processes, can initiate ionization or other reactions, leading to damage at the regions where local field maxima occur. Without clear knowledge of the $|E|^2$ distributions and of how those distributions affect the damage behavior of nodules, it is impossible to gain a true understanding of LID initiating from nodules.

The focusing effect of the domed nodules first comes to mind, and Murphy [28] has suggested that the domed nodules might act as microlenses focusing the laser light and thereby causing local damage. However, he assumed an average dielectric constant for the HR coating. Dijon et al. further improved the microlens model by considering the reflectivity distribution over the surface of nodules [26]. The angle of incidence differs from the nominal angle when the point of incidence moves from the center to the edge of a nodule. And the thickness of the coated layers on the nodule edge somewhat deviates from the designed thickness due to the shadowing effect during deposition. As a result, the light may penetrate through HR coatings along the nodular edge. Then the nodule tends to act as a microlens that focuses light, as shown in Figure 8.

The microlens model is very simple and should be qualitatively correct. However, it is certainly very crude

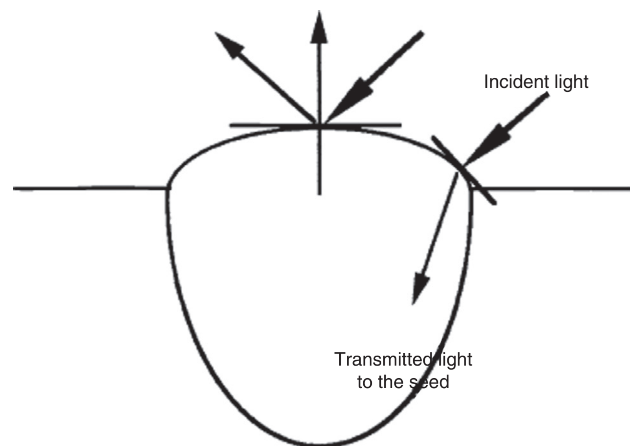

Figure 8 Proposed explanation for an enhanced transmission of the mirror above the seed. On the edge of the nodule, the angle of incidence of the light is very different from the nominal angle of the mirror due to the spherical shape of the defect (reproduced from Dijon et al. [26]).

because no diffraction effect or interference effect is taken into consideration for the close ratio of the nodular diameter to the laser wavelength. A numerical solution is the more appropriate approach dealing with such a complicated problem. DeFord and Kozlowski made the first finite difference time domain (FDTD) model of E-field enhancement in nodular defects and demonstrated that a nodule could result in an E-field enhancement that was 3.5 times higher than the incident E-field strength [29]. However, their code limited calculations to rotationally symmetric two-dimensional cases only and also neglected polarization effects. Stolz et al. first clearly demonstrated that a nodule was exposed to a range of incident angles and to opposite polarizations at orthogonal cross-sections [30], and thus only a three-dimensional (3D) FDTD code could sufficiently mimic the E-field enhancement in nodules. Because this concept is critical to the understanding and interpretation of the FDTD simulation results, we will briefly restate their classic work here. A theoretical nodule is created by depositing a quarter-wave reflector design [air:L(LH)^{12}:glass] over a 1 μm spherical seed. The nodular geometry is selected as D=sqrt(8dt) by assuming uniform deposition over the spherical seed. Given the hemispherical shape of the defect, the nodular defect has an angular range defined by Equation (1):

$$\phi=2\cos^{-1}\left[\frac{2t-d}{2t+d}\right] \quad (1)$$

where t is the film thickness and d is the seed diameter. At normal incidence to the defect-free region of the coating, the incidence-angle range (θ) of the defect is shown in Equation (2):

$$0\leq\theta\leq\frac{\phi}{2} \quad (2)$$

Even for normal incidence cases, polarization effects become significant, as illustrated in Figure 9. A nodule exposed to a linearly polarized laser beam is actually exposed to both 'S' and 'P' polarization (TE and TM) at orthogonal cross-sections. And the angular reflection bandwidths (ARBs) of the HR coating is very different for 'S' and 'P' polarization, which directly affects the percentage of light penetration through the nodule edge and the resulting E-field enhancement. Thus, only a 3D FDTD modeling can realize polarization effects and give the right simulation results.

Using a 3D FDTD code, Stolz et al. carried out in-depth studies [31, 32] to investigate the dependence of E-field enhancement on seed properties, incident angle, centering wavelength, etc. Here we give several examples. Figure 10 shows the simulation results of a series of D=sqrt(8dt) nodules that were created from deeply embedded seeds. For the normal incidence case, light intensification increases with increasing inclusion diameter. For the 45° incidence case, light intensification does not show a strong dependence on inclusion diameter. Simulations were performed from 20° to 60° to obtain the influence of incident angle on light intensification. Interestingly, maximum light intensification occurred at 25°. Some of the observed dependences can be explained by a comparison between the incident angular range (IAR) of a nodule and the ARB of HR coatings, whereas other dependences still cannot be simply explained. Other reasons, such as resonant effect, may play a role here [33]. Figure 11 shows the E-field intensity distributions of a nodule as a function of wavelength, incident angle, and polarization, where light intensification focal spots shift away from the central axis with increasing incidence angle. For the same defect geometry, wavelength changes lead to very different electric field profiles and light intensification magnitudes.

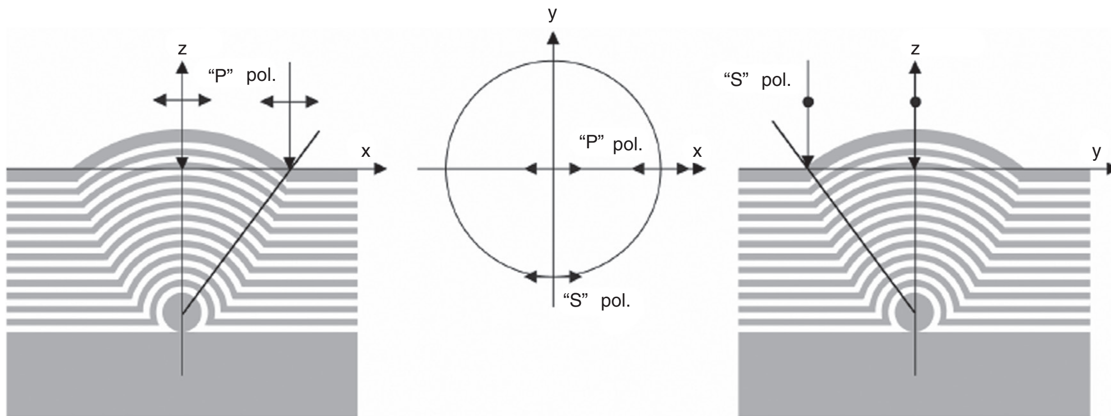

Figure 9 Normal incidence irradiation of a nodular defect has different polarization orientations for orthogonal cross-sections (reproduced from Stolz et al. [30]).

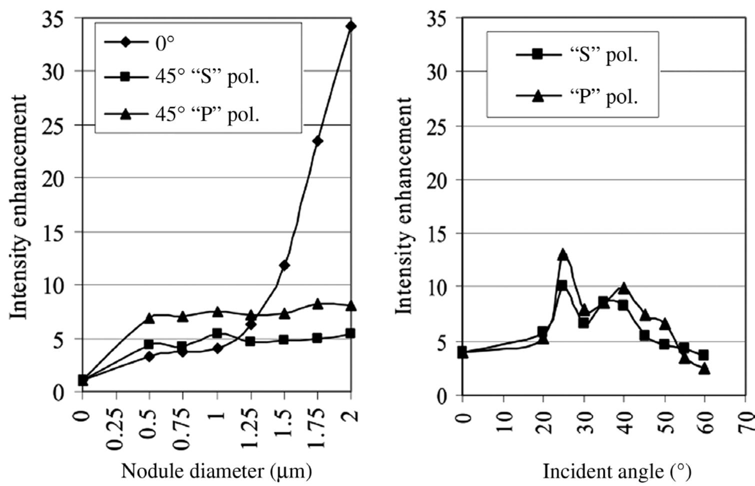

Figure 10 Light intensification of a deeply embedded inclusion (24 layers) as a function of spherical inclusion diameter, incidence angle, and polarization (left-hand panel) and as a function of incident angle and polarization for a constant spherical inclusion diameter of 1.0 µm (right-hand panel) (reproduced from Stolz et al. [32]).

Their simulation results revealed the dependence of E-field enhancement on the properties of the nodule, which helps in knowing which types of nodules are more dangerous from the viewpoint of laser damage resistance, and helps in guiding the optimization of the deposition process.

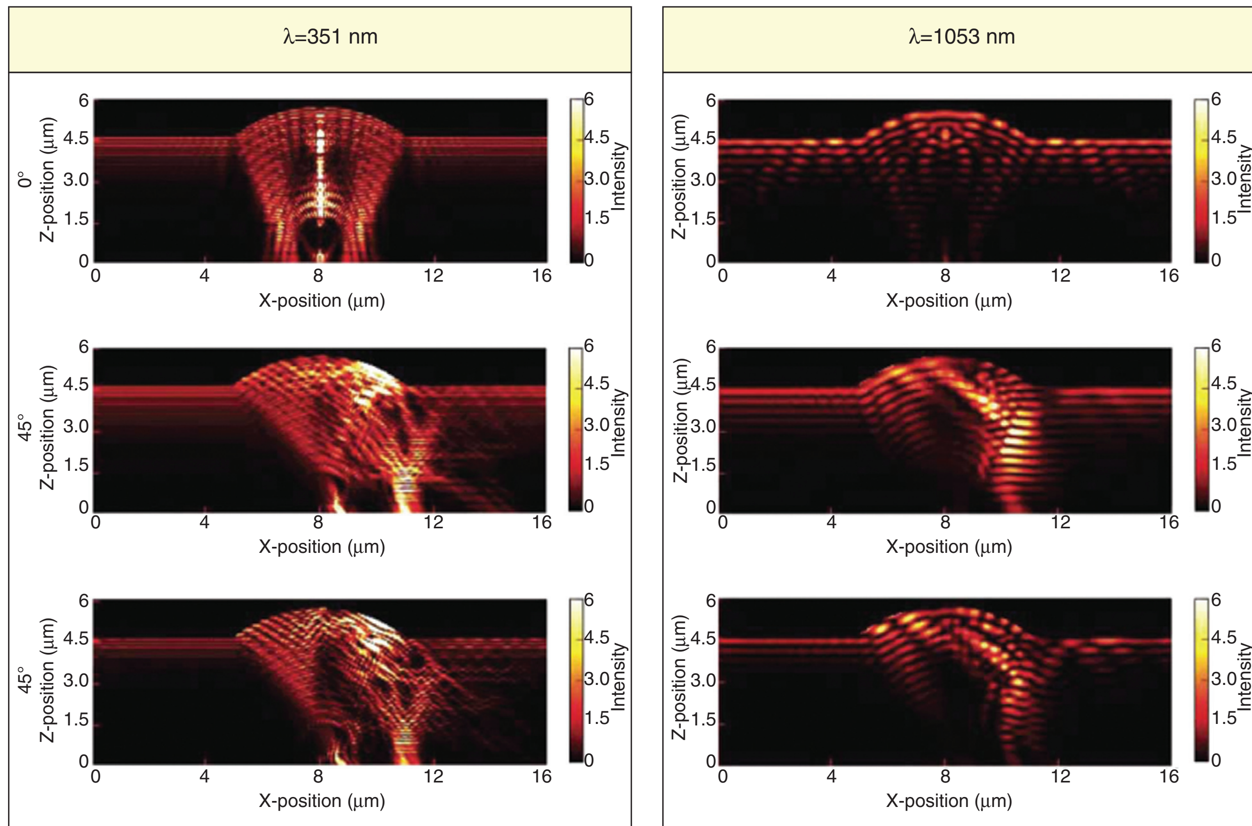

Figure 11 Light intensification simulations of a coating nodule with a 1 µm diameter inclusion as a function of wavelength, incident angle, and polarization (reproduced from Stolz et al. [32]).

However, E-field simulations of nodules are far from comprehensive. Nodules with different aspect ratios have been reported [17, 34], but systematic studies of 3D FDTD modeling of E-fields in nodules have been limited to a *D*=sqrt(8*dt*) geometry. The influence of nodular geometries on E-field enhancement is still not very clear. Moreover, the correctness of E-field simulation results has not been directly proven from experimental results, which prevents the achievement of a clear understanding of the damage process of nodular defects and restricts detailed studies of subsequent thermal, stress, and mechanical simulations. A recent advance achieved by us has shown excellent agreement between the damage morphologies and the simulated $|E|^2$ distributions of artificial nodules [35]. Two types of nodular, as shown in Figure 2, were systematically and comparatively studied to reveal the dependence of E-field distribution on nodular geometries and then to show how E-field distributions affect the damage behavior of nodules.

First, the *D*=sqrt(4*dt*) nodules were studied and compared to the widely studied *D*=sqrt(8*dt*) nodules. Figure 12 presents the geometric modeling of nodules used for electric field simulations. For *D*=sqrt(4*dt*) nodules, the resulting layers that form above the seed are tangent spheres, and the point of tangency is the intersection point between the spherical seed and the substrate surface. For *D*=sqrt(8*dt*) nodules, the resulting layers that form above the seed are concentric spheres. An interesting finding is that the IAR of the *D*=sqrt(4*dt*) aspect ratio nodules is much larger than that of the *D*=sqrt(8*dt*) aspect ratio nodules for the same seed diameter. And the IAR of bigger nodules for both geometries is already larger than the P-polarization ARB of the HfO_2/SiO_2 HR coating that is designed to work at normal incidence. Because the two nodular geometries have different IARs, the portion of the laser beam that can penetrate through the multilayer stack will be different, probably resulting in different E-field enhancement.

Figure 13 shows the P-polarized $|E|^2$ distributions for the two nodular geometries initiating from 0.3, 0.6, 0.9, 1.45, and 1.9 μm silica microspheres. The differences between the $|E|^2$ distributions for the two nodular geometries are dramatic. For the *D*=sqrt(8*dt*) nodular geometry, $|E|^2$ distributions calculated by our FDTD code are very similar to the results given by Stolz et al., where the maximum $|E|^2$ was located at the upper central axis of the nodules. Compared to the *D*=sqrt(8*dt*) nodular geometry, the *D*=sqrt(4*dt*) nodular geometry results in very different $|E|^2$ distributions. The positions of the $|E|^2$ maxima are much deeper and even occur within the seeds for the larger nodules. Moreover, the *D*=sqrt(4*dt*) nodular geometry also leads to much higher $|E|^2$ enhancement than the *D*=sqrt(8*dt*) nodular geometry. The observed differences in the $|E|^2$ distributions can be primitively explained from the aspect of the different IARs of the two nodular geometries. However, the focusing or resonance effects may also play a role. More work is needed to achieve a better understanding of $|E|^2$ enhancement in nodules.

To find out whether the simulated $|E|^2$ distributions are correct and to reveal how the $|E|^2$ distributions affect the thermomechanical damage of nodules, the artificial nodules were damaged by a nanosecond-pulsed laser and an FIB instrument was used to examine the cross-sectional damage morphologies of the ejected nodules. Figure 6 shows that nodules initiating from the 0.3 and 0.6 μm non-absorbing silica seeds could not be damaged at the maximum fluence of our laser damage test facility, thus our interest here is mainly in the vulnerable nodules initiating from bigger seeds. Figure 14 shows the damage morphologies of nodules initiating from 0.9, 1.45, and 1.9 μm silica seeds. The damage morphologies in the left-hand column are considered to be the representative ones. Upon careful examination of the damage morphologies of the nodules initiating from the 1.9 and 1.45 μm seeds, we reached the conclusion that the silica seeds were not

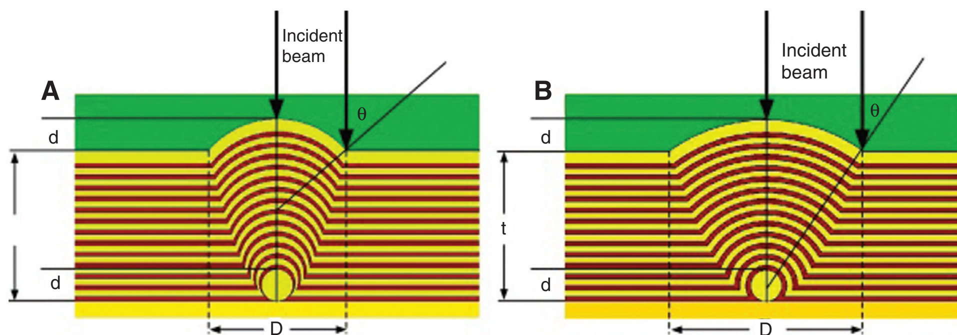

Figure 12 The geometries of nodules initiating from a 0.9 μm silica microsphere that were used for electric field simulations. (A) Nodule with a *D*=sqrt(4*dt*) aspect ratio, (B) nodule with a *D*=sqrt(8*dt*) aspect ratio [35].

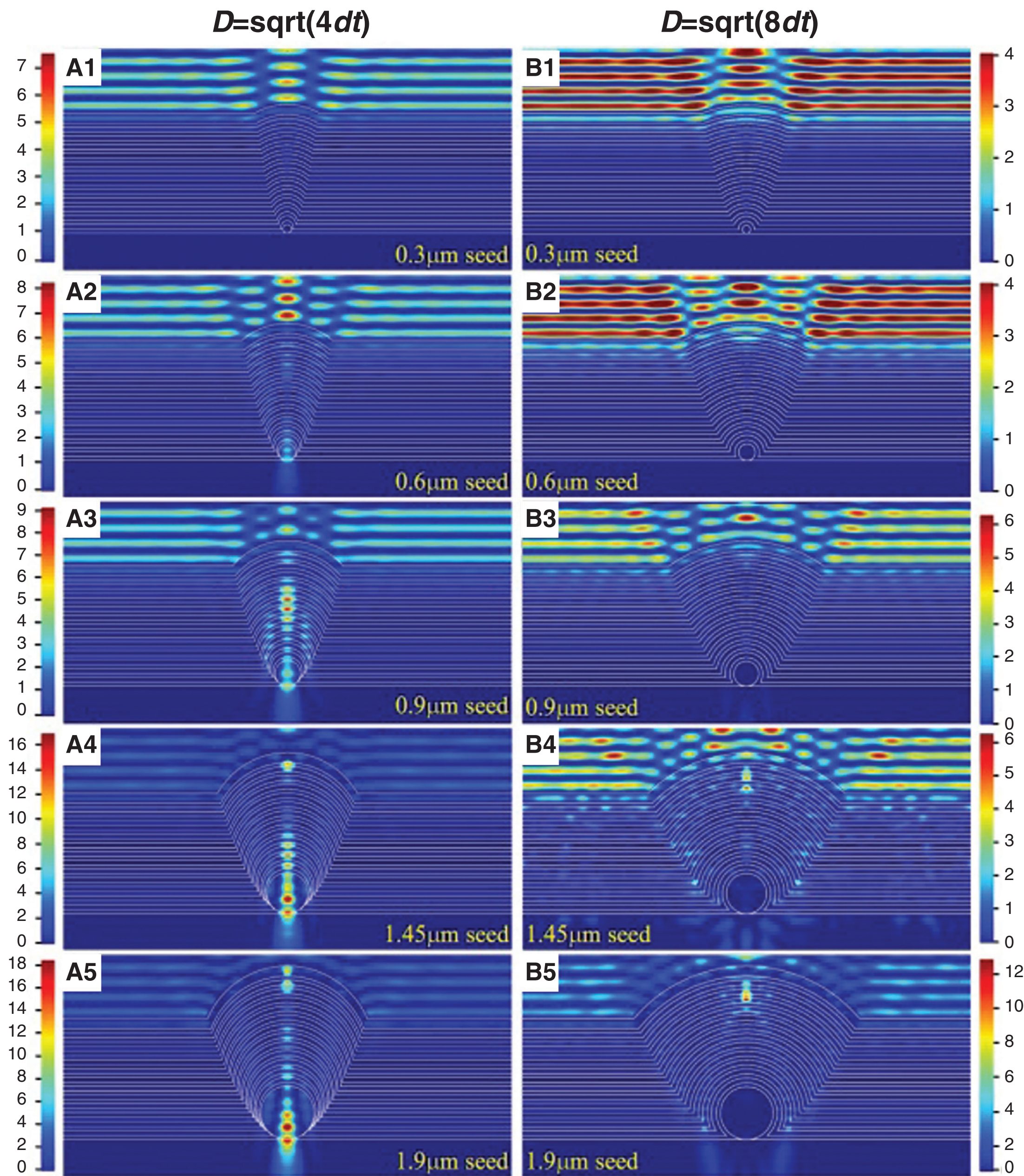

Figure 13 FDTD-simulated P-polarized $|E|^2$ distributions: (A1–A5) for the *D*=sqrt(4*dt*) nodular geometry and (B1–B5) for the *D*=sqrt(8*dt*) nodular [35].

ejected but rather melted. Only when strong light intensification occurs in seeds, as is the case in our simulation results, can such melting-like damage morphologies occur for silica seeds whose absorption is extremely low. Interestingly, for the damage morphology of the nodule initiating from the 0.9 μm silica seed, the nodule was not ejected along the most unstable boundaries, that is, in the vicinity of the seed, but was instead ejected from the upper, more continuous boundaries. We can infer that the initial damage originated at the middle region of the film stack where the coating materials melted due to intense $|E|^2$, in agreement with the simulation results. Although we attempted to make identical nodules by creating them from monodisperse silica microspheres, the ejection fluences and damage morphologies of nodules initiating from the same-sized seeds still exhibited some

differences. The images in the right-hand column of Figure 14 show the complexity of nodular damage. These damage morphologies did not show a good relationship with simulated $|E|^2$ distributions and were thought to be unrepresentative. For example, the 1.9 μm seed did not melt when the film stack was ejected along the boundaries, the 1.45 μm seed did not show obvious melting-like damage morphology, and there was no evidence that the initial damage started from the middle of the film stack for the nodule initiating from the 0.9 μm seed. We think that the main reason for this complexity is the poor mechanical stability of nodules prepared via EBE. When there is fluctuation in the seed diameter, a slight variation of seed absorption or some other unknown changes, mechanical instability will combine the impact of all fluctuations and result in different damage morphologies, which actually have a negative effect on our judgment of the impact of $|E|^2$ distributions on nodular damage. Because FIB measurement is very expensive and time-consuming, it is impossible to ascertain the representative damage morphologies by exposing a large number of nodules. Therefore, we prepared another series of nodules to more efficiently demonstrate the influence of $|E|^2$ distributions on their damage behaviors. The basic idea was to make the boundaries more continuous to reduce the influence of mechanical instability. Meanwhile, film absorption

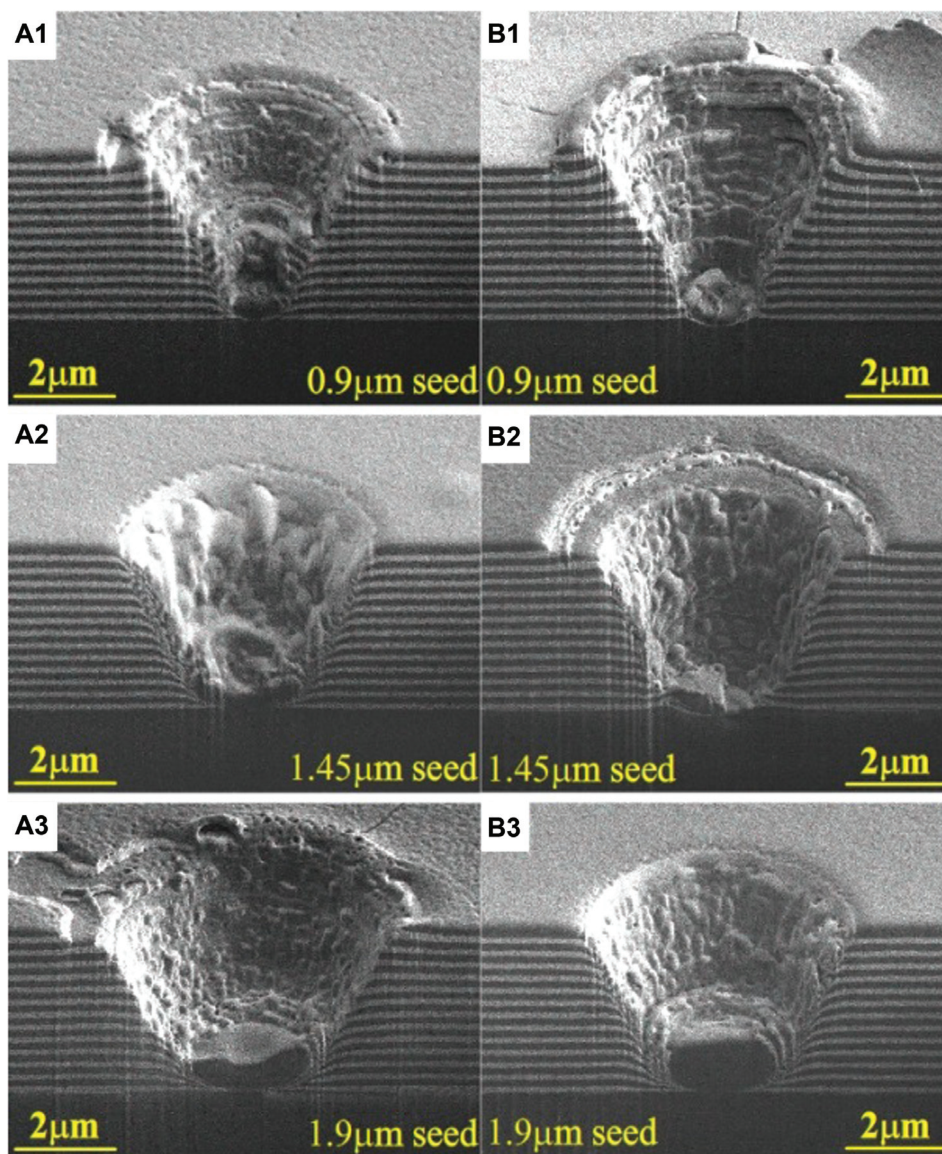

Figure 14 Damage morphologies of nodules revealed by FIB technology. (A1–A3) Damage morphologies that exhibited good agreement with the simulated $|E|^2$ distributions. (B1–B3) Damage morphologies that showed some deviation from the simulated $|E|^2$ distributions [35].

was purposely increased to amplify the contribution of the electric field to nodular damage. The D=sqrt(2.5dt) nodules that were prepared by the IAD process, as shown in Figure 5, are good examples for further confirming that a direct link between $|E|^2$ distributions and damage morphologies exists.

For HR coatings prepared by the IAD process, the ejection of nodules created from 0.3 μm seeds always occurred with catastrophic damage, and it was impossible to find or inspect subtle damage morphologies of ejected nodules. Here, we investigated the link between $|E|^2$ distributions and damage morphologies of nodules initiating from 0.6, 0.9, 1.45, and 1.9 μm silica seeds. Figure 15 shows the P-polarized $|E|^2$ distributions and the corresponding nodular damage morphologies. The most obvious change of the $|E|^2$ distributions for

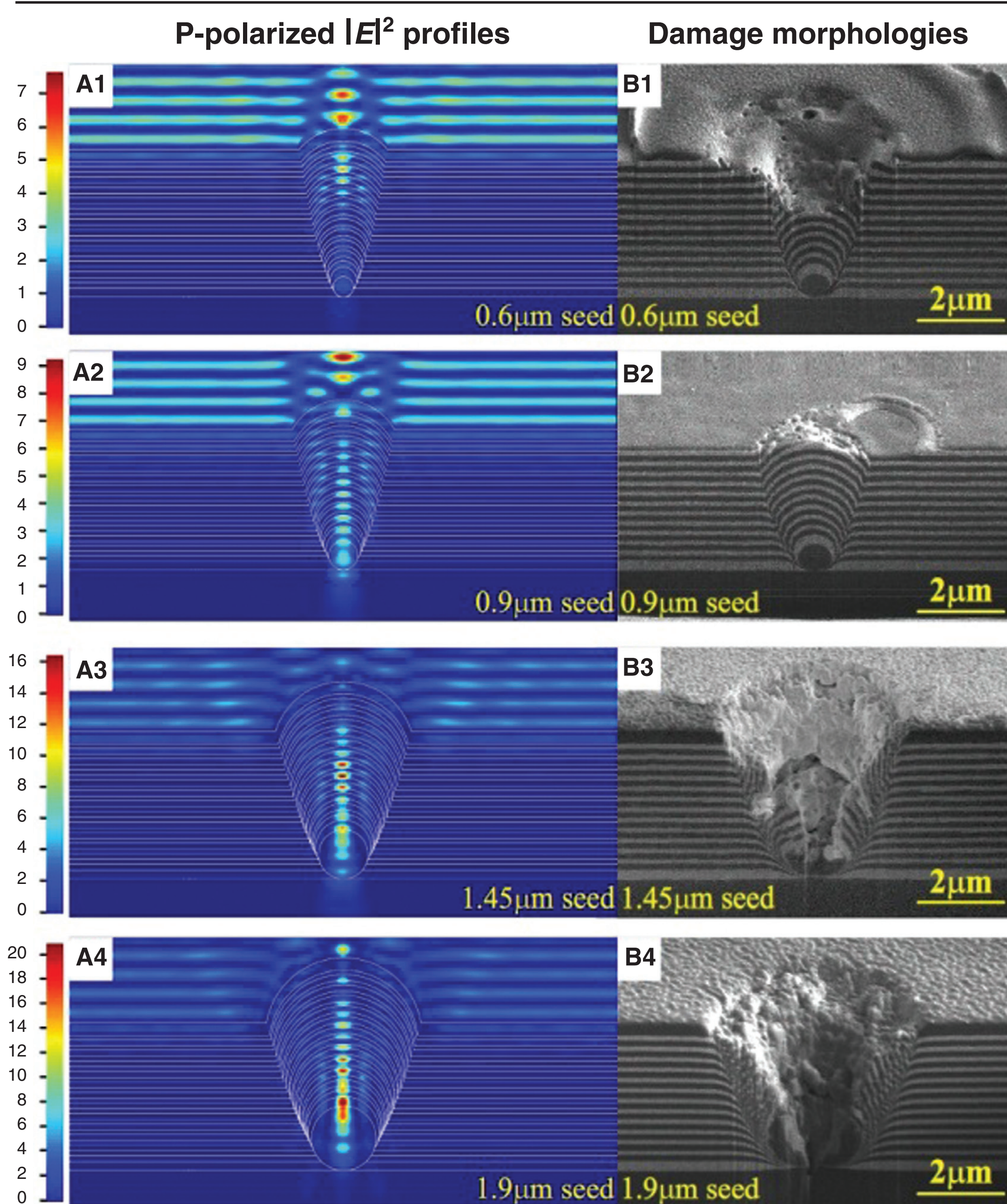

Figure 15 Comparisons between simulated $|E|^2$ distributions and the damage morphologies of nodules prepared via the IAD process. (A1–A4) FDTD-simulated P-polarized $|E|^2$ distributions, (B1–B4) damage morphologies [35].

the D=sqrt(2.5dt) geometry is that the peak $|E|^2$ positions shift upward by some distance compared to the D=sqrt(4dt) geometry. Now, most strong $|E|^2$ regions are located within the film stack. Because the film absorption is much higher now, the impact of E-field on nodular damage will be amplified. The damage morphologies of nodules initiating from 1.9 and 1.45 μm seeds have two notable features. The first is that neither the seeds nor deeper layers were melted, but rather were cut apart in the middle. The second is that the film stack was not ejected along existing boundaries, but was destroyed around the central part of the film stack. These features can be perfectly explained from the aspects of $|E|^2$ distributions, film absorption, and mechanical stability. The absorbed heat or temperature increase is determined by the combined effect of $|E|^2$ and film absorptions. Because the absorption of films prepared via IAD is much higher than that of the seeds, the temperature peak will occur in the film stack according to the simulated $|E|^2$ profiles. Moreover, the temperature gradient and stress response will be much more localized to the $|E|^2$ distributions due to the high absorption of the films. The film stack melts first, and then a strong tensile stress is generated along the axis of the nodules, which is intense enough to cut open either the deep layers or the seeds. Because boundary continuity was significantly improved during IAD, the coating materials are merely sprayed out near the melting region rather than at the boundaries. Nodules initiating from 0.9 μm seeds also show unique damage morphologies, with only the top several layers being destroyed. This result is in excellent agreement with the simulated $|E|^2$ profiles in which the positions of peak $|E|^2$ are only located in the top several layers. As for the nodules initiating from the 0.6 μm seeds, the strong $|E|^2$ positions are located in the upper part of the film stack, so, naturally, the upper part of the film stack is melted and destroyed.

For a series of nodules prepared via the EBE and IAD processes, the damage morphologies almost completely reproduce the $|E|^2$ distributions, which convincingly prove the correctness of the $|E|^2$ simulations and also demonstrate exactly how $|E|^2$ distributions affect the damage morphologies of the nodules. Our findings provide more information on the damage process of the nodules and lay a good foundation for subsequent thermal, stress, and mechanical simulations. Pre-existing thermal-mechanical modeling of nodular defects, including temperature gradient, associated stress, state changes (such as melting), material removal, etc., can be further improved with detailed knowledge of the damage morphologies of ejected nodules.

2.2.1.4 Solutions to control nodular defects

Nodules initiating from particulates on the surface of substrates are addressed first. The cleaning of substrate surfaces is important in the manufacture of all types of high quality coatings. The common cleaning methods, such as swab and solvent, detergent and water cleaning, ultrasonic cleaning, laser-assisted particle removal, etc., have been reviewed by Bennett [36]. In addition, the inspecting methods for assessing cleaning efficiency, including visual inspection using the naked eye or a magnifying glass, dark field or Nomarski microscope, total internal reflection microscopy, total integrated scattering or angle-resolved scattering, etc., were also discussed. For the manufacture of high LIDT coatings, ultrasonic aqueous cleaning, with or without mechanical scrub, is the most commonly used technique. Further discussions are devoted to ultrasonic aqueous cleaning. The particles are removed from the surface by the combined effects of chemical etching, a net repulsive interaction between the particles and surface, and the mechanical force that is exerted by the imploding of small bubbles created by the ultrasonic energy [37]. The acoustic boundary layer thickness, corresponding to the diameter of particles that can be most efficiently removed, is determined by Equation (3):

$$d=\sqrt{2\nu_1/\omega} \tag{3}$$

where ν_1 is the kinematic viscosity of the solution and ω is the ultrasonic frequency. As the diameter of particles decreases, the ultrasonic frequency needs to be increased to remove them effectively. It is also important not to use too intense and/or long-term ultrasonic agitation because surfaces can be roughened by the combined action of etching by the solutions and the mechanical effect of the ultrasound. Poor cleaning is much worse than no cleaning. The optics industry uses a variety of specialized ultrasonic processes to clean optical surfaces. A cleaning protocol presented by Rigatti is provided as an example to show how sophisticated the high-level cleaning process is [38]. The process includes four main steps. A detailed process flow chat is presented in Figure 16.

Splattering from the evaporation source is another type of seed to form nodules. Here we limit our discussion to the case of HfO_2/SiO_2 coatings prepared by the EBE process. When HfO_2 are used as the evaporating materials, most nodules in HfO_2/SiO_2 coatings initiated from splattered HfO_2 seeds that are created due to the temperature-induced phase transformation of the HfO_2 material [39]. Between the cooled edges of the HfO_2 plug in contact with the water-cooled crucible and the molten surface in contact with the electron beam, HfO_2 undergoes

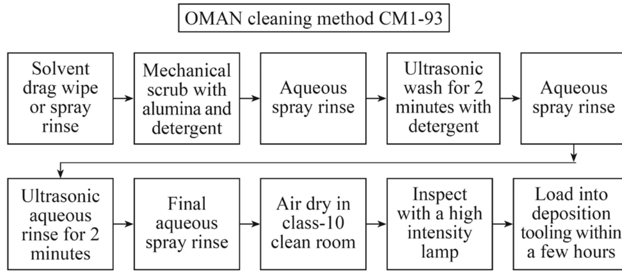

Figure 16 LLE cleaning method CM1-93 (reproduced from Rigatti [38]).

a monoclinic-to-tetragonal phase transformation near 1700°C resulting in a 3.8% volumetric expansion that can produce lots of particle ejections. An important technological breakthrough in manufacturing high damage threshold coatings is to prepare HfO_2 layers from a metallic Hf source in a reactive environment [40]. Hf has higher thermal and electrical conductivity than HfO_2 and has no temperature-induced phase transformations, the defect density drops by a factor of 3–10, with the majority of nodular seeds now of SiO_2 composition.

It is also challenging to avoid silica spattering during evaporation due to its poor thermal and electrical conductivities. Some key deposition parameters, such as e-gun voltage, e-gun emission current, sweep pattern, and dwell time, etc., can be adjusted to reduce particle ejections from the SiO_2 evaporation source [41, 42]. It has been reported that an arc suppressor unit could suppress anomalous electric discharges (arcing) during electron beam evaporation, which will directly help to maintain the stability of deposition rate and reduce the spattering from the SiO_2 source [15]. Filtering of ejected particles from the evaporation source, using electrostatic defection, rotating fans, baffles, and gas jet momentum control, have been proposed [39]. Although the success of the filtering concept has been limited, future technical progress may achieve the full potential of these techniques [43].

Although deposition and cleaning technologies evolve quickly, it is still impractical to eliminate all the seeds that can initiate nodular defects; alternative solutions need to be developed. Stolz et al. recently demonstrated a planarization technique to deal with nodules initiating from engineered pillars [44]. Based on the fact that the ion beam etching rate of SiO_2 is slower at higher incident angles, pillars were overcoated with a planarization layer utilizing a smoothing process consisting of successive SiO_2 deposition and etching. When the planarization layer is thick enough, a near-perfect mirror coating can be deposited on the planarized surface. The geometric minimization of coating defects significantly improves the laser resistance to more than 100 J/cm^2 (10 ns pulse length). The planarization effectiveness is clearly seen in the cross-sectional micrograph of 1 μm tall, 2 μm diameter cylindrical pillars, as shown in Figure 17.

Laser conditioning of dielectric thin film coatings at exposure levels below the catastrophic laser damage threshold has been widely used to increase the functional LIDT [45]. Although the mechanisms for laser conditioning are not completely understood, gentle nodular ejection has been accepted as the main mechanism to improve the functional laser damage resistance of HfO_2/SiO_2 multilayer coatings working at 1064 or 1053 nm. Gentle nodular ejection can be viewed as benign damage which does not create dangerous plasmas modifying properties of coating materials or leading to delaminations of layers. Benign nodular ejections leave smooth-edged pits that are mechanically more stable than nodules. Moreover, FDTD simulations show that E-field enhancement in coatings with smooth-edged pits is also much weaker compared to that in coatings with nodules [46], as shown in Figure 18. Thus, benign nodule ejection pits can survive much higher fluences and the pits are not inclined to grow with repetitive irradiations.

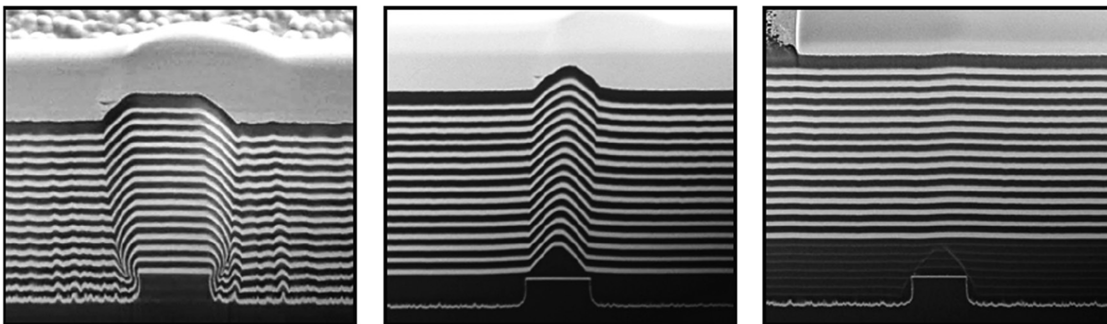

Figure 17 Control defect (left), 1 μm thick planarization layer (center), and 2 μm thick planarization layer (right) (reproduced from Stolz et al. [44]).

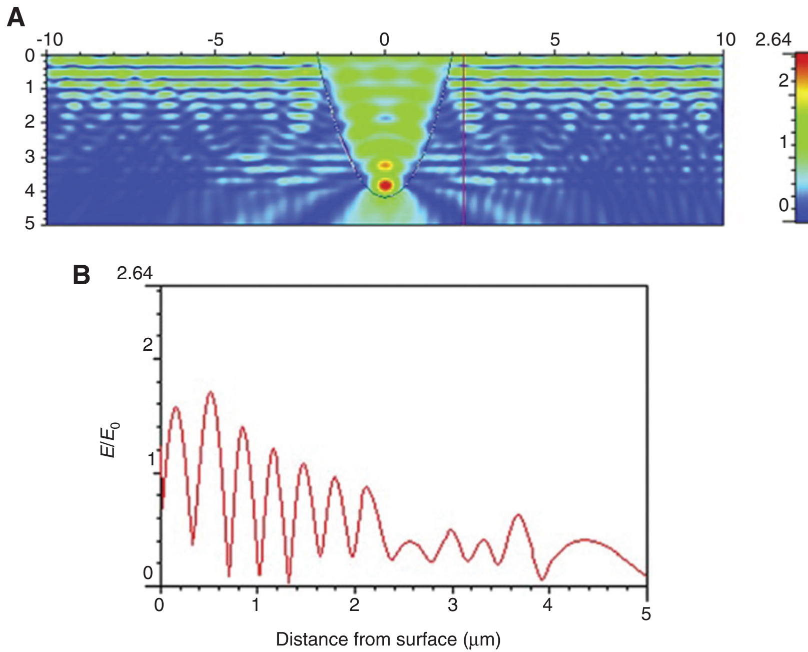

Figure 18 (A) The E-field distribution within HR coatings with a pit, which is 4 μm in diameter and 4.2 μm in depth. (B) The simulated field strength profile along film depth at the edge of the pit as marked in (A) by the red line (reproduced from Shan et al. [46]).

2.2.2 Defects originating from substrate imperfections

For fusion-scale laser systems, the substrate diameter is over half a meter. Severe scratches on such huge substrates are inevitably created with current polishing technologies. The influence of scratches on LID of antireflection coatings is very similar to the case of bare substrates [47, 48], which will not be discussed here. The scratch-induced laser damage in HR coatings will be discussed here with emphasis on the dependence of LIDT on scratch characteristics and the mechanisms that lead to LID.

Qiu et al. have combined experimental approaches with theoretical simulations to delineate the correlation between laser damage resistance of coating layers and the properties of pre-engineered scratches on BK7 substrates [21]. The scratches with widths ranging from 15–30 μm, 30–45 μm, to 45–60 μm were created by dragging the sample surface across a pad that contained imbedded

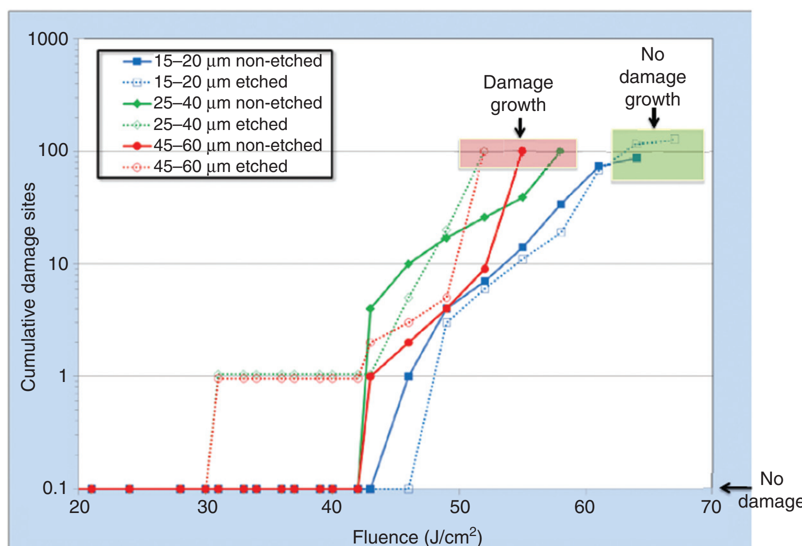

Figure 19 Laser damage initiation and growth threshold for HR coating on BK7 substrate with surface scratches of different widths (reproduced from Qiu et al. [21]).

silica spheres. Some scratches were also etched to check whether this technique, which works very well for transparent optics, is also applicable to HfO_2/SiO_2 HR coatings that are prepared by the EBE process. Although this technique creates scratches in a similar matter to grinding or polishing, the absence of polishing and cutting residues means that it cannot mimic real scratches completely. What this technique does provide is nominally uniform and reproducible scratches for the reliable study of LID. The damage testing results for samples with different scratch widths are summarized in Figure 19. The initiation fluence for all three scratch widths (non-etched) is the same at ~42 J/cm^2. The growth threshold depends on the scratch width; the smaller the scratch width, the higher the fluence required for the damage site to grow. For scratch widths larger than 25 μm, etching of the substrate before coating reduced the damage threshold. Scratches narrower than 20 μm did not generate growing or propagating damage sites over the range of fluences tested in this study.

LID initiating from scratch-perturbed HR coatings can be interpreted with regard to mechanical properties and $|E|^2$ enhancement. Figure 5A shows that the layers growing on wide scratches are not continuous. Their thermomechanical stability is much worse than perfect films. When laser irradiation induces a strong temperature gradient and associated stress, thermomechanical damage initiates preferentially at these unstable scratch-perturbed structures. E-field modeling can also provide insight into LID initiating from scratch-perturbed structures. The distribution of $|E|^2$ is simulated using the FDTD method based on the cross-sectional image of the coatings growing on a substrate-etched sleek (Figure 20A). Figure 20B shows that light intensification as high as 4 times exists in the top layer of the coating, which indicates that damage could happen at a lower damage threshold compared to a defect-free region of the coating. Light intensification at scratch-perturbed structures apparently depends on the shape of the scratch on the substrate. Etching widened the scratches, resulting in a larger area of the coating that modulated the electric field, and leading to higher magnitude intensification. Stronger E-field enhancement may thus be the reason why etching of the substrate before coating reduces the laser damage resistance.

To minimize surface scratches and subsurface damage in optical substrates, conventional processes, such as grinding, lapping, bowl-feed polishing, float polishing, etc., have been re-optimized, and new technologies, such as magnetorheological polishing, fluid jet polishing, laser polishing, etc., have been proposed and developed to improve the surface and subsurface quality beyond any

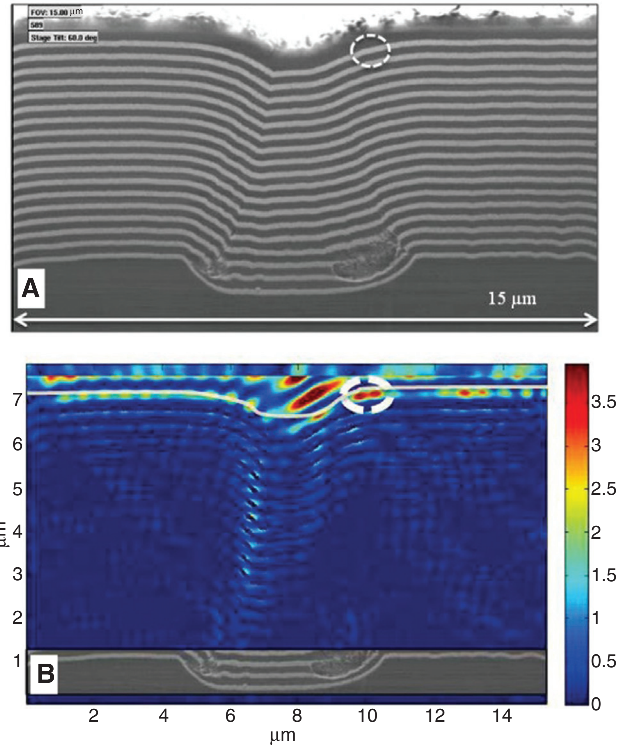

Figure 20 (A) Cross-sectional SEM images of HR coatings growing on a sleek. (B) Distribution of E-field intensification within scratch-distorted coating (reproduced from Qiu et al. [21]).

level previously attained. Detailed discussion of polishing is beyond the scope of this review. More materials can be found in the SPIE conference series: Laser-Induced Damage in Optical Material.

2.3 The influence of defects on other properties of optical coatings

2.3.1 Scattering

Scattering from localized defects in optical coatings can severely degrade the performance of high-precision optical systems. For example, modern image detection systems commonly employ optical coatings immediately in front of detector arrays, which is particularly susceptible to the scattering of coating defects because light leakage through a defect is not averaged out over the whole detector array but is imprinted upon the pixel directly beneath it. For the special case where a band-pass filter is mounted before the detector, the out-of-band rejection dropped by as much as three orders of magnitude as the filter was brought from the far field to a position directly in front of a detector [49]. This phenomenon is known as the Stierwalt effect and is caused by scattering from defects in

filters. Moreover, the evolution of high-sensitivity applications has pushed the total loss of optical coatings to the ppm level. Among different loss mechanisms, light loss due to scattering is usually pronounced. Except for roughness, the presence of a few localized defects in the coatings could be a significant source of scattering loss [3]. Although numerous studies have explored the dependence of scattering loss on surface roughness, interface correlation, and bulk irregularities [50–58], only a few studies have investigated scattering from defects [59–64]. To narrow the scope of this section, only recent advances on scattering from defects on single surfaces are reviewed.

Zerrad et al. have presented a very good numerical analysis to show the impact of localized defects on scattering and the deduced root mean square (rms) roughness [65]. They considered a low roughness plane silica surface that was illuminated by a collimated beam at the wavelength λ=847 nm in air. The bidirectional reflectance distribution function (BRDF) calculated from the clean surface profile as a function of the scattering angle θ is given in Figure 21. The rms roughness of this surface was deduced to be 0.865 nm. They then numerically added some isolated dome-shaped defects to this surface with random diameters between 3 and 8 μm and height <0.2 μm, and whose refractive index was the same as the surface. The red line in Figure 21 shows that the BRDF level was significantly increased by the presence of ten defects on the surface. Moreover, Figure 22 shows that the rms roughness of this same surface increased as the number of defects on the sample surface was increased. These numerical results show that the determination of the rms roughness of a surface through a scattered intensity measurement can very quickly become inaccurate because of the presence of a few localized defects on the surface.

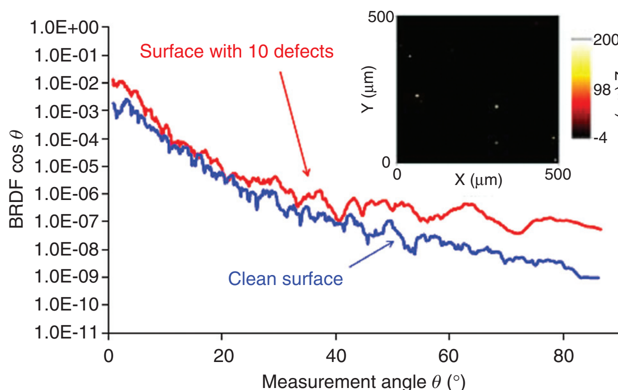

Figure 21 Influence of ten localized dome-shaped defects on light scattering from a 500 μm×500 μm² surface (reproduced from Zerrad et al. [65]).

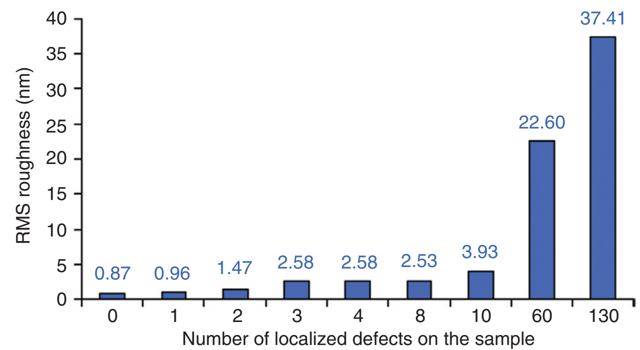

Figure 22 Root mean square (rms) roughness of the surface with different numbers of isolated defects (reproduced from Zerrad et al. [65]).

Herffurth et al. presented a different approach using a compact CMOS sensor matrix to measure the 3D angle-resolved scattering (ARS) from nano-roughness or small defects [66]. One merit of their measurement system is that the compact light-scatter sensor and a white light interferometer (WLI) (ZYGO New View 7300) can be integrated into one stage, which makes it possible to record 3D surface profiles of defects at the same positions where the ARS measurements are performed. The right column in Figure 23 shows the topography profiles recorded with the WLI of a scratch and a particle on an RG1000 substrate, as well as two defects on a silicon surface with a 200 nm Ti thin film. The images in the left column show the corresponding ARS patterns measured with the light-scatter sensor. It is clear that defects on the substrate surface or in the coatings give rise to strong and anisotropic scattering. Especially for Figure 23C, an inverse correlation between the defect diameter and angle between the first minimum and the specular reflected beam becomes visible. Additionally, they also used the Beckmann-Kirchhoff theory to further investigate the estimation of the sizes of pits in the surfaces from the ARS distributions. The system not only can measure the scattering from defects but can also deduce the dimensions of defects based on a scattering map.

2.3.2 The reflected field of EUV coatings

EUV lithography uses a reflective mask consisting of a glass substrate, a multilayer reflective coating, and a patterned absorber layer. The EUV light reflected by the mask is imaged onto the wafer. The reflected field must be uniform in both amplitude and phase to avoid producing critical errors in the lithographic image of the mask pattern. Defects, such as scratches, nodules, or pits, can

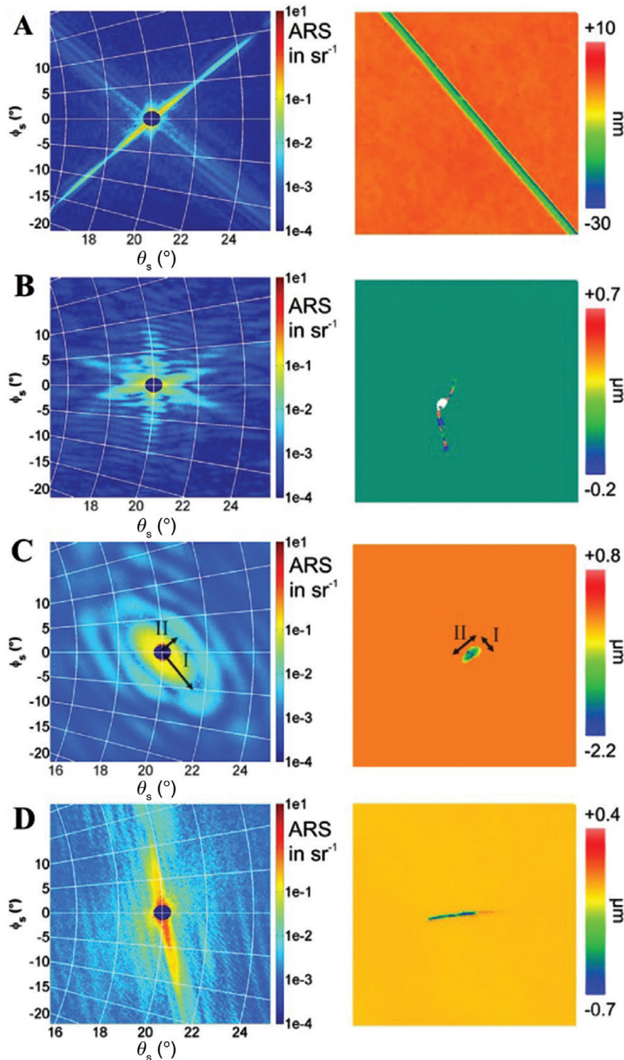

Figure 23 Selected defects. Left: angle-resolved scattering (ARS). Right: corresponding white light interferometer (WLI) topography data (scan area: 370 µm×370 µm). I and II label the axes and the corresponding scatter features of pit 'C' (reproduced from Herffurth et al. [66]).

cause a local modulation of the reflected field and thus produce large errors in the printed features, which are usually called printable defects [4]. Taking an exposure tool operating at a wavelength of 13.5 nm and having a numerical aperture of 0.25 as an example, a defect is printable if its height at the surface of the coating is >2 nm. Such a requirement is rather challenging. What is worse is that standard inspection techniques cannot identify such small features. Stearns et al. demonstrated a smoothing method that used an etching process to decrease the defects nucleated by 50 nm particles to a diameter below 1 nm when the multilayer coating is deposited [4]. They also developed a non-linear continuum model to simulate the growth of localized defects in multilayer coatings. Figure 24 shows good agreement between the TEM image of the shrunk defects and the corresponding simulation results. For protruding defects, the incorporation ion beam etching into the multilayer deposition process proved to be effective, although other cases, such as scratches and pits, were not addressed. Subsequently, Sugawara et al. investigated the printability of a scratch defect onto the substrate surface by simulations [20]. They assumed that no excess atoms were supplied to fill a scratch defect, thus the cross-sectional area of smoothing and non-smoothing deposition should be the same. The smoothing deposition causes the topography of a defect to laterally expand and vertically contract from the bottom to the top of a multilayer, as shown in Figure 2. Their simulation results reflected that such a shallower and wider topography caused bigger inhomogeneities in the phase of the reflected field, which makes the scratch more printable. In practice, whether the smoothing or non-smoothing approaches should be used depends on the properties of the defects in the coatings.

2.3.3 Mechanical and environmental stability

Localized stress can be created in coatings where non-homogeneous growth occurs around defects in the film. When the localized stress exceeds the fracture toughness of the coatings, localized adhesion failure, causing flaking or cracking, will occur. Figure 25 shows the fracture of an electron beam evaporated HfO_2/SiO_2 coating [67]. A nodular defect in the coating provides an initiation site for tensile stress failure, while tearing of the film is evident within the crack that forms. Defects also enhance moisture penetration in optical coatings exposed to a hygrothermal environment, which is very critical for coatings on susceptible substrates, such as hygroscopic crystals, optical grade polymers, etc. Moisture absorption in the vicinity of defects in optical coatings induces additional stresses within the coatings and ruins the substrate surface, which can cause interfacial delamination and subsequent cracking of the multilayer. Even for BK7 substrates, defect-induced failure of optical coatings has been reported [5]. Figure 26 shows an area of coating delamination and its relationship with defects. An initial generation position for the failure at the bottom of the delaminated area can be clearly seen in Figure 26.

3 Non-visible absorbing defects

The morphologies of some damage sites as well as their laser damage behaviors suggest that LID of optical coatings

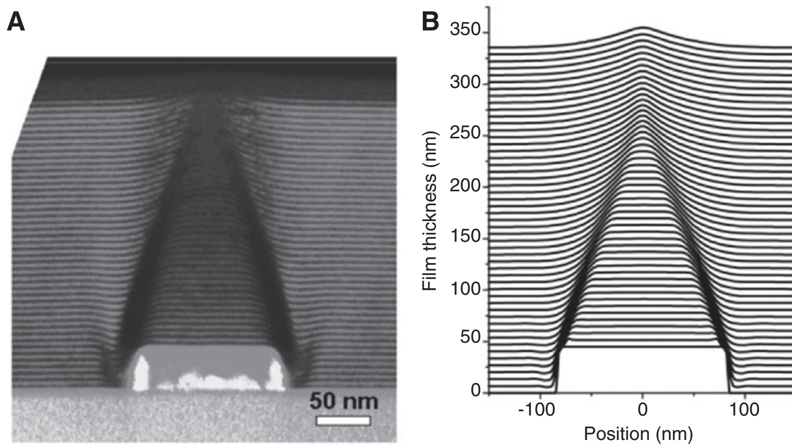

Figure 24 (A) Cross-sectional transmission electron microscope image of a defect in the Mo/Si multilayer coating nucleated by a lithographically patterned particle with a width of 165 nm and height of 45 nm. The dark layers are Mo. (B) Simulated layer structure through the middle of the defect (reproduced from Stearns et al. [4]).

in the nanosecond regime is initiated by localized nano-absorbing defects. For the widely used HfO_2/SiO_2 combination, metallic Hf nano-clusters, off-stoichiometric HfO_2 nano-clusters, or areas of high-density electronic defects have been speculated as possible sources for triggering LID [68, 69]. Real nano-absorbing defects are still not detectable with current technology due to their very small size and localized property. The question on the nature of nano-absorbing defects remains open. The connection between nano-absorbing defects and coating properties has not been established, which hampers the optimization of deposition processes to improve laser damage resistance. Currently, laser damage analysis is the only way to explore nano-absorbing defects, but this approach is destructive and only limited information about the nano-absorbing defects can be obtained. Based on the measured laser damage probability as a function of the parameters of the laser beam, the size and/or density of different nano-absorbing defects can be deduced. According to the detailed knowledge of damage morphologies, mechanisms for laser damage initiating the nano-absorbing defects have also been proposed.

3.1 Phenomenological studies according to damage probability

LID initiating from nano-absorbing defects is localized and probabilistic. Statistics for the nano-absorbing

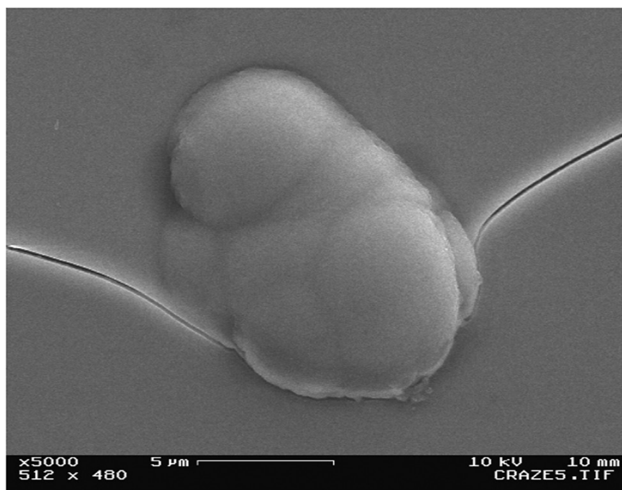

Figure 25 SEM imaging of the initiation site and crack that forms as a result of the high tensile stress in an evaporated hafnia/silica film (reproduced from Oliver et al. [67]).

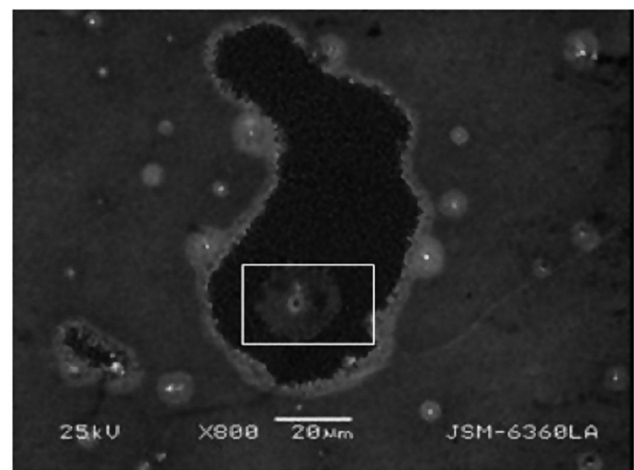

Figure 26 Pinhole defect induced filter failure, and the box shows the pinhole defect site (reproduced from Zhang et al. [5]).

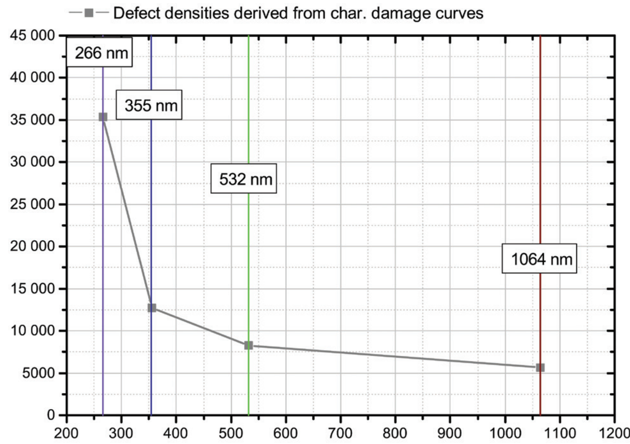

Figure 27 Estimated defect density as a function of test laser wavelength (reproduced from Jensen et al. [71]).

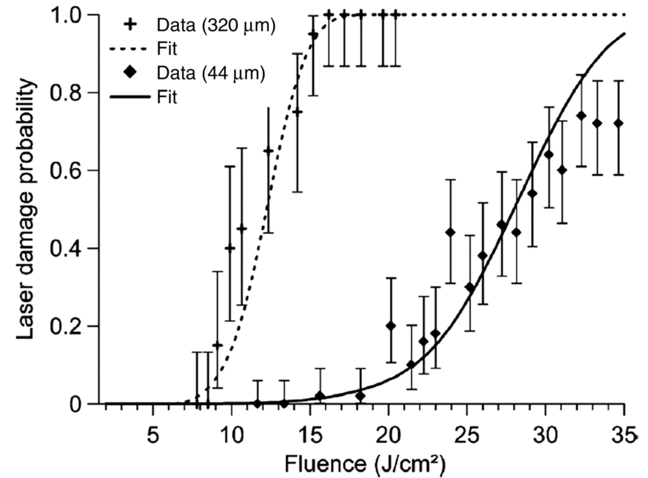

Figure 29 Laser damage probability measured (at 1064 nm/12 ns) for a hafnia film. The calculated curves are plotted for the same values of fit parameters for both beam sizes (reproduced from Gallais et al. [72]).

defects can be obtained by determining the dependence of laser damage probability on fluence, beam diameter, wavelength, etc. Assuming that damage occurs if a nano-absorbing defect is present in the irradiated area where the laser fluence is higher than the threshold fluence of this defect, the damage probability can be calculated theoretically by knowing the size distribution of defects and then compared to experiments [70].

Among the various questions arising, whether the nature and density of the nano-absorbing defects change with wavelength is of particular interest. Jensen et al. performed detailed investigations on the laser damage probability of HfO_2/SiO_2 high reflectors as a function of the spot size at four different wavelengths, that is, 1064, 532, 355, and 266 nm [71]. Considering that HfO_2/SiO_2 high reflectors have a limited density of nano-absorbing defects, laser damage probability should reduce with the decreasing spot size of the test laser beam. At a specific spot size, the beam will most likely not hit any coating defects and the damage threshold will be governed by the intrinsic properties of coating. If the damage threshold fluence as a function of the spot size is plotted, this specific spot size should be the turning point where the damage threshold suddenly increases. Obviously, this specific spot size is inversely proportional to the density of nano-absorbing defects. The spot size at which the slope of the curve increases sharply differs greatly between the four wavelengths. The specific beam diameters are 60, 100, 120, and 150 μm, respectively, for 266, 355, 532, and 1064 nm, which corresponds to different defect densities at different wavelengths, as shown in Figure 27. The densities of defects should not be considered to be absolute. The order of magnitude and the difference between the four wavelengths can give an indication that UV laser pulses hit a larger number of defects. There are two possible reasons for the observed trend suggesting that films have higher density of defects at shorter wavelengths. One is that new sources of defects emerge at shorter wavelengths and they create more defects; another is that additional transient defects are generated by UV laser irradiation.

The morphologies of the damaged sites that were irradiated by UV laser pulses were compared for small and large beam diameters. Larger density of nano-absorbing defects led to more craters within the beam profile, as shown in Figure 28B,D. There are much higher defect

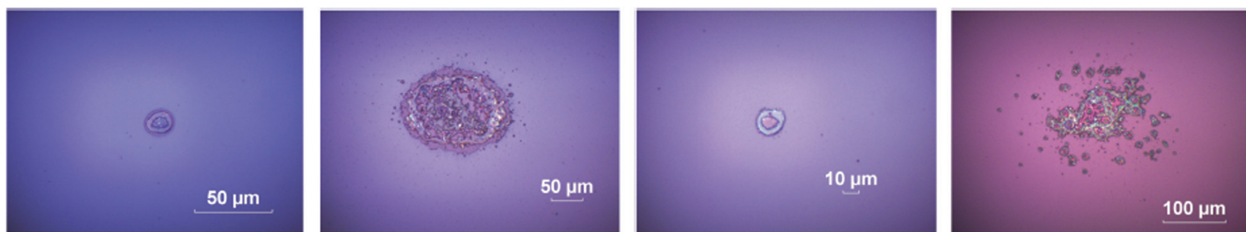

Figure 28 Damaged sites of single shot damage tests: (A) 355 nm to 22 μm, (B) 355 nm to 154 μm, (C) 266 nm to 26 μm, (D) 266 nm to 340 μm (reproduced from Jensen et al. [71]).

densities in the UV region compared to the visible or near IR regions. The damage morphologies of all craters given in Figure 28 were very similar, and the localized defect-driven damage mechanism needs to be explored to discover the crater formation process.

Usually, such phenomenological studies cannot show the physical and chemical nature of the nano-absorbing defects; Gallais et al. attempted to relate the nature of the defects to the measured laser damage probability [72]. Under certain assumptions, they proposed a model to link the measured laser damage probabilities to the properties of the nano-absorbing defects, such as defect composition, the size distribution of defects, and their density. Their model is based on the calculation of light absorption in defects and subsequent heating. When information of a given type of nano-absorbing defect is coupled with laser damage statistics, laser damage probability as a function of laser fluence can be calculated. They considered metallic Hf nano-clusters and non-stoichiometric HfO_2 defects as potential nano-absorbing defects in HfO_2, and assumed a power law distribution for these defects. The HfO_2 single layer that was prepared using reactive low voltage ion plating was tested by 1064 nm, 12 ns pulses from an Nd:YAG laser. Figure 29 shows that the measured threshold was 8 J/cm^2 in the case of the 320 μm spot size and 15 J/cm^2 in the case of the 44 μm spot size. Under their assumptions, dielectric defects could not trigger laser damage at the fluence of 8 J/cm^2. When using a defect size distribution between 5 and 55 nm, very good agreement was obtained between the experimental value and the theoretical data, as shown in Figure 29. Hf defects of a few tens of nanometers were considered to be potential defects. Their model can describe the observed spot size dependence and fit two sets of data simultaneously using the same parameters, which support the effectiveness of their method to some extent. However, the deduced results must be considered with caution because several assumptions have been made for the calculations. The interest of their approach may not be to identify certain defects but to highlight potential candidates.

3.2 Interpretation of crater formation

The experimental study of nano-absorbing defect-driven LID has been very restricted owing to two reasons. The first is that the physical nature of the real nano-absorbing defects in optical coatings is still not completely known, and the second is that it is very difficult to carry out reproducible experiments using real nano-absorbing defects. Many experiments have shown that the damage morphologies initiating from real and artificial nano-absorbing defects are very similar. Thus, an alternative approach to study laser interaction with nano-absorbing defects is to introduce artificial nano-absorbing defects inside the coatings [73–75]. Gold nanoparticles are the preferred choice for artificial absorbing defects because of their well-known optical and thermal characteristics, chemical stability, and availability in the form of gold colloids or powders. Most studies on LID initiating from artificial nano-absorbing defects have been conducted using a UV nanosecond pulse laser. By exploring the damage behaviors of SiO_2 layers embedded with gold nanoparticles, Papernov and Schmid have proposed a phenomenological model of crater formation [76]. This model involves four steps.

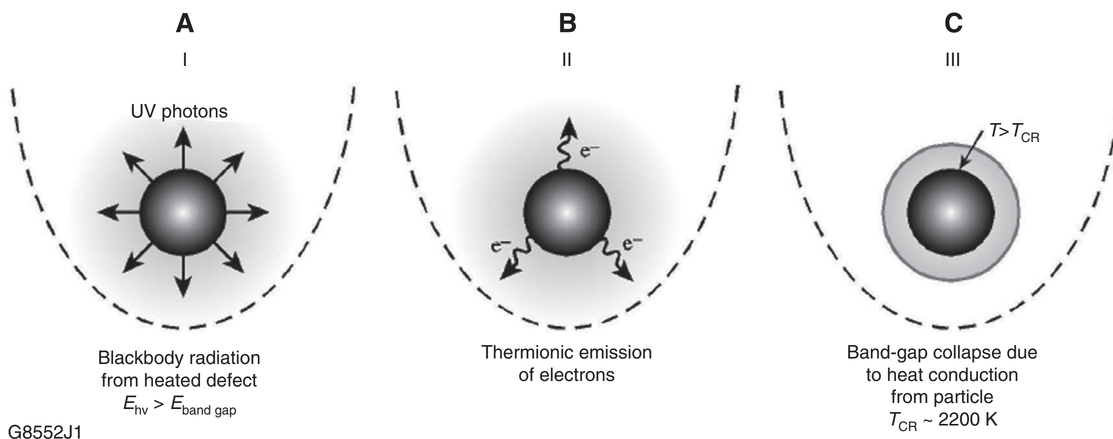

Figure 30 Schematic presentation of three mechanisms transforming the absorber-surrounding matrix into absorbing medium: (A) photoionization by UV radiation from the heated absorber; (B) thermionic emission of electrons; and (C) heat transfer-induced band gap collapse (reproduced from Papernov and Schmid [76]).

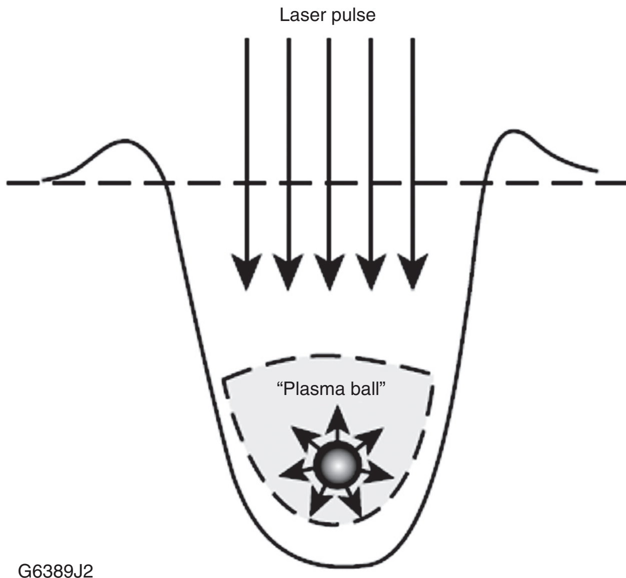

Figure 31 Schematic of the plasma ball formation around an absorbing defect (reproduced from Papernov and Schmid [76]).

– **Heating of the nano-absorbing defects** The energy absorbed by an isolated nano-absorbing defect can be calculated using Mie theory. Due to its very small size and lower thermal conductivity than the film matrix, the defect itself can reach very high temperature and pressure. However, calculations show that, considering the energy absorption process is localized inside the defect, the amount of energy absorbed is insufficient to form micron-sized craters [77].
– **Energy transfer from heated nano-absorbing defects to surrounding film matrix** A critical role in the damage kinetics is played by the energy transferred from the heated particle to the surrounding film matrix. Three possible mechanisms converting the transparent dielectric coating into an absorbing medium are identified [76], as shown in Figure 30. First is the photo-ionization by the UV photons of the black-body radiation from the heated defects; the second approach is via the thermionic emission of electrons from the heated defects; and the third is due to matrix band gap collapse upon reaching a critical temperature at the absorber/matrix interface.
– **Heating of the surrounding absorbing matrix by laser** The rapid heating and ionization of the surrounding matrix by laser leads to the formation of a plasma 'fire ball' with an energy density well above the evaporation energy, as shown in Figure 31. The plasma ball radius grows exponentially with laser fluence F. At high laser fluences, the growth of the plasma ball tends to saturate and its diameter reaches a maximum value of the order of λ. In this case the absorbed energy can be estimated as $E=F\pi\lambda^2$ [78].

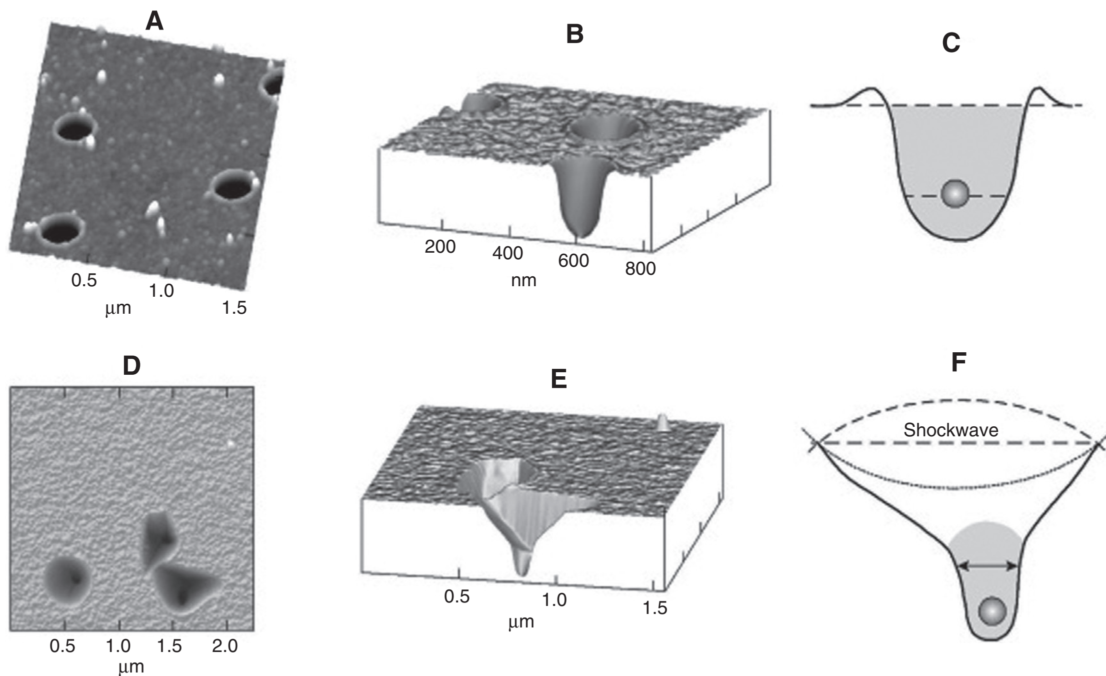

Figure 32 Characteristic crater morphologies produced by 351 nm, 0.5 ns irradiation of 18.5 nm particles lodged at different depths: (A) regular crater, surface plot, 60 nm absorber lodging depth; (B) cross-sectional view of regular crater; (C) schematic presentation of the melt front inside the regular crater; (D) complex crater, surface plot, 190 nm absorber lodging depth; (E) cross-sectional view of the complex crater; (F) schematic presentation of the melt front and shock wave inside the complex crater (reproduced from Papernov and Schmid [76]).

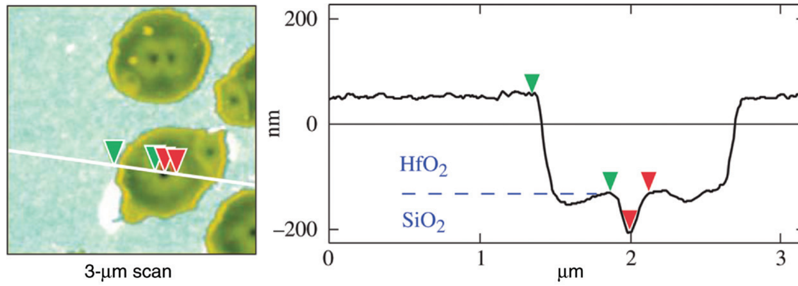

Figure 33 Damage crater cross-sectional profile (atomic force microscope). The crater depth measurement points to the removal of the hafnia layer within the crater volume (reproduced from Papernov et al. [68]).

– **Thermomechanical effects** Both pure thermal (melting and vaporization) and thermomechanical (fracture generation) effects must be taken into consideration to describe and predict the final crater formation. Using an atomic force microscope, two types of damage crater morphology were found in SiO_2 coatings with 18.5 nm gold particles lodging at different depths. Craters resulting from melting and evaporation usually have a single-cone shape, as shown in Figure 32A–C. Such craters are usually formed at relatively shallow absorber locations, where the melt front accompanying the plasma ball front reaches the material surface. Another type of crater exhibits a complex structure with a double-cone cross-sectional profile having a random lateral shape, with sharp corners, as seen in Figure 32D–F. This second crater morphology is usually observed when the absorber lodging depth exceeds some critical value. The upper portion of the crater may be removed by fracture. Thus, complex crater formation involves a combination of melting and fracture.

Papernov et al. further investigated the interfacial damage between HfO_2 and SiO_2 layers in the UV region [68]. The cross-sectional profiles of the damage site are shown in Figure 33. The damage at the center of the crater propagates 30–80 nm into the underlying SiO_2 layer, which indicates the melting and removal of the silica layer. They hypothesized the following damage process: nano-absorbing defects in the HfO_2 layer first absorb energy from the laser pulse; those heated defects that are also adjacent to the SiO_2 layer can transfer heat to the silica; considering that the melting point of HfO_2 [$T_m(HfO_2)$=3085 K] is much higher than the melting point of SiO_2 [$T_m(SiO_2)$=1986 K], SiO_2 material is first heated up to the melting point and becomes absorptive; the local temperature and pressure can grow dramatically by acquiring energy from the laser pulse; and the HfO_2 material is removed from the crater without full melting, via a stress-driven mechanism. Such a damage mechanism might also be relevant to any HfO_2/SiO_2 multilayer coatings irradiated by a UV nanosecond pulse laser, which helps to explain the morphologies of the craters thus formed.

Understanding of LID initiating from nano-absorbing defects has been deepened by these studies, but opportunities for improving the understanding of the mechanisms of localized defect-driven damage are far from exhausted. More importantly, the physical nature of real nano-absorbing defects still cannot be ascertained, new non-destructive characterization techniques having nanometer resolution may be the next critical step to deal with this issue.

4 Summary and perspectives

Defects in optical coatings can degrade their performance in many ways. Which types of defects should be controlled and to what degree they should be controlled depends on the application and the understanding of defect-related properties in optical coatings. The challenging aspects of dealing with defects include: the nature and properties of defects are not completely known; defects are localized, with low numbers and low density; and their properties, including absorption, size, depth, etc., probably vary from defect to defect. Taking high power laser coatings as an example, such a complex situation hampers the experimental and theoretical studies of defect-driven LID in optical coatings. Using artificial defects whose damage behavior is similar to real defects is an effective approach to systematically study defect-driven LID in optical coatings. New or deeper understanding of LID initiating from nodules or nano-absorbing defects has been achieved, which helps

to re-optimize existing technologies and to develop new processes to control these defects and to further increase laser damage resistance.

Optical coating is a technology domain driven by application. As modern optical systems evolve, the requirement of our understanding of defect-related properties and the ability to control defects are steadily increased. There is enough room for scientific and technological progress on defect-related properties in optical coatings. Here, only a few suggestions are proposed for future studies.

- Except for eliminating the sources of defects, new technologies that can weaken the influence of existing defects are highly desirable [4, 20, 44].
- Non-destructive localized characterization techniques can be improved to achieve nanometer scale resolution and even to highlight band gap or electronic defects [79, 80].
- Studies that can distinguish scattering from localized defects and interfacial roughness in multilayer coatings with large effective detection area should be conducted.
- Studies of localized mechanical properties and stress state in the area of defects can be further investigated.

Acknowledgments: This work was partly supported by the National Natural Science Foundation of China (grant numbers 61235011, 61008030, 61108014, 61205124). The authors are grateful to our colleagues for their support and Norbert Kaiser for the invitation to write this review.

Received December 14, 2013; accepted January 16, 2014

References

[1] G. Kolodnyi, V. Azarova, Y. Golyaev, A. Melnikov, M. Rasyov, et al., Proc. SPIE 3738, 446 (1999).
[2] T. Accadia, F. Acernese, F. Antonucci, P. Astone, G. Ballardin, et al., Astroparticle Phys. 34, 521–527 (2011).
[3] S. Maure, G. Albrand and C. Amra, Appl. Optics 35, 5573–5582 (1996).
[4] D. G. Stearns, P. B. Mirkarimi and E. Spiller, Thin Solid Films 446, 37–49 (2009).
[5] D. P. Zhang, J. D. Shao, H. J. Qi, M. Fang, K. Yi, et al., Opt. Laser Technol. 38, 654–657 (2006).
[6] C. J. Stolz, Proc. SPIE 6834, 683402 (2007).
[7] D. Besnard, Eur. Phys. J. D 44, 207 (2007).
[8] H. W. Yu, F. G. Jing, X. F. Wei, W. G. Zheng, X. M. Zhang, et al., Proc. SPIE 7131, 713112 (2009).
[9] A. M. Ledger, Appl. Opt. 18, 2979–2989 (1979).
[10] K. H. Guenther, Appl. Opt. 20, 1034–1038 (1981).
[11] M. J. Brett, R. N. Tait, S. K. Dew, S. Kamasz and A. H. Labun, J. Mater. Sci. Mater. 3, 64 (1992).
[12] C. J. Stolz, L. M. Sheehan, M. K. Gunten, R. P. Bevis and D. J. Smith, Proc. SPIE 2714, 374 (1999).
[13] L. Dubost, A. Rhallabi, J. Perrin and J. Schmitt, J. Appl. Phys. 78, 3784 (1995).
[14] S. A. Letts, D. W. Myers and L. A. Witt, J. Vac. Sci. Technol. 19, 739 (1981).
[15] X. B. Cheng, Z. X. Shen, H. F. Jiao, J. L. Zhang, B. Ma, et al., Appl. Opt. 50, C357–C363 (2011).
[16] X. F. Liu, D. W. Li, Y. A. Zhao and X. Li, Appl. Opt. 49, 1774–1779 (2010).
[17] X. B. Cheng, T. Ding, W. Y. He, J. L. Zhang, H. F. Jiao, et al., Proc. SPIE 8190, 819002 (2011).
[18] B. J. Liao, D. J. Smith and B. McIntyre, NBS SP 746, 305 (1987).
[19] T. Suratwala, R. Steele, M. D. Feit, L. Wong, P. Miller, et al., J. Non-Cryst. Solids 354, 2023–2037 (2008).
[20] M. Sugawara, I. Nishiyama, K. Motal and J. Cullins, Jpn. J. Appl. Phys. 45, 9044–9052 (2006).
[21] S. R. Qiu, J. E. Wolfe, A. M. Monterrosa, W. A. Steele, N. E. Teslich, et al., Proc. SPIE 7842, 78421X-1 (2010).
[22] M. C. Staggs, M. R. Kozlowski, W.J. Siekhaus and M. Balooch, Proc. SPIE 1848, 234 (1992).
[23] A. Bodemann, N. Kaiser, M. Kozlowski, E. Pierce and C. Stolz, Proc. SPIE 2714, 395 (1996).
[24] M. Poulingue, J. Dijon, B. Rafin, H. Leplan and M. Ignat, Proc. SPIE 3738, 325 (1999).
[25] C. Y. Wei, K. Yi, Z. X. Fan and J. D. Shao, Appl. Opt. 51, 6781–6788 (2012).
[26] J. Dijon, M. Poulingue and J. Hue, Proc. SPIE 3578, 387 (1998).
[27] M. Poulingue, M. Ignat and J. Dijon, Thin Solid Films 348, 215–221 (1999).
[28] J. K. Murphy, Proc. SPIE 246, 64 (1980).
[29] J. F. DeFord and M. R. Kozlowski, Proc. SPIE 1848, 455 (1993).
[30] C. J. Stolz, F. Y. Génina and T. V. Pistor, Proc. SPIE 5273, 41 (2004).
[31] C. J. Stolz, M. D. Feit and T. V. Pistor, Appl. Opt. 45, 1594–1601 (2006).
[32] C. J. Stolz, M. D. Feit and T. V. Pistor, Appl. Opt. 47, C162–C166 (2008).
[33] V. E. Gruzdev and A. S. Gruzdeva, Proc. SPIE 3263, 169 (1998).
[34] Y. G. Shan, H. B. He, C. Y. Wei, S. H. Li, M. Zhou, et al., Appl. Opt. 49, 4290–4295 (2010).
[35] X. B. Cheng, J. L. Zhang, T. Ding, Z. Y. Wei, H. Q. Li, et al., Light Sci. Appl. 2, e80 (2013).
[36] J. M. Bennett, Proc. SPIE 5273, 195 (2004).
[37] Z. X. Shen, T. Ding, X. W. Ye, X. D. Wang and B. Ma, Appl. Opt. 50, C433–C440 (2011).
[38] A. L. Rigatti, Proc. SPIE 5647, 136 (2005).
[39] M. R. Kozlowski and R. Chow, Proc. SPIE 2114, 640 (1994).

[40] C. J. Stolz, L. M. Sheehan, M. K. Gunten, R. P. Bevis and D. J. Smith, Proc. SPIE 3738, 318 (1999).
[41] R. Chow and N. Tsujimoto, Appl. Opt. 35, 5095–5101 (1996).
[42] N. Wang, J. D. Shao, K. Yi and C. Y. Wei, Chin. Opt. Lett. 8, 621 (2010).
[43] J. E. Wolfe, C. J. Stolz and S. Falabella, Opt. Interf. Coat. Techn. Digest FA.2 (2013).
[44] C. J. Stolz, J. E. Wolfe, P. B. Mirkarimi, J. A. Folta, J. J. Adams, et al., Opt. Interf. Coat. Techn. Digest FA.1 (2013).
[45] H. Bercegol, Proc. SPIE 3578, 421 (1999).
[46] Y. G. Shan, H. B. He, Y. Wang, X. Li, D. W. Li, et al., Opt. Commun. 284, 625–629 (2011).
[47] P. E. Miller, J. D. Bude, T. I. Suratwala, N. Shen, T. A. Laurence, et al., Opt. Lett. 35, 2702–2704 (2010).
[48] T. I. Suratwala, P. E. Miller, J. D. Bude, W. A. Steele and N. Shen, J. Am. Ceram. Soc. 94, 416–428 (2011).
[49] J. D. Barrie, P. D. Fuqua, B. L. Jones and N. Presser, Thin Solid Films 447, 1–6 (2004).
[50] C. Amra, C. Grézes-Besset and L. Bruel, Appl. Opt. 32, 5492–5503 (1993).
[51] C. Amra, J. H. Apfel and E. Pelletier, Appl. Opt. 31, 3134–3151 (1992).
[52] E. L. Church, H. A. Jenkinson and J. M. Zavada, Opt. Eng. 18, 125 (1979).
[53] J. Stover, 'Optical Scattering – Measurement and Analysis', 2nd ed. (SPIE, Washington, 1995).
[54] M. Trost, S. Schröder, T. Feigl and A. Duparré, Appl. Opt. 50, C148–C153 (2011).
[55] J. M. Elson, J. P. Rahn and J. M. Bennett, Appl. Opt. 19, 669–679 (1980).
[56] P. Bousquet, F. Flory and P. Roche, JOSA 71, 1115–1123 (1981).
[57] A. Duparré, in 'Encyclopedia of Modern Optics', Ed. by B. D. Guenther, D. G. Steel and L. Bayvel (Elsevier, Amsterdam, 2004) pp. 314–320.
[58] S. Schröder, T. Herffurth, H. Blaschke and A. Duparré, Appl. Opt. 50, C164–C171 (2011).
[59] R. P. Yang, Opt. Eng. 15, 516 (1976).
[60] K. B. Nahm and W. L. Wolfe, Appl. Opt. 26, 2995–2999 (1987).
[61] T. A. Germer, Appl. Opt. 36, 8798–8805 (1997).
[62] J. C. Stover, V. Ivakhnenko and Y. A. Eremin, Proc. SPIE 4449, 131 (2001).
[63] S. Schröder, M. Kamprath and A. Duparré, Proc. SPIE 5878, 232 (2005).
[64] A. Okamoto, H. Kuniyasu and T. Hattori, IEEE Trans. Electr. Devices, 19, 372 (1999).
[65] M. Zerrad, M. Lequime, C. Deumié and C. Amra, Proc. SPIE 7102, 710207-1 (2008).
[66] T. Herffurth, S. Schröder, M. Trost, A. Duparré and A. Tünnermann, Appl. Opt. 52, 3279–3287 (2013).
[67] J. B. Oliver, P. Kupinski, A. L. Rigatti, A. W. Schmid, J. C. Lambropoulos, et al., Opt. Express 20, 16596–16610 (2012).
[68] S. Papernov, A. Tait, W. Bittle, A. W. Schmid, J. B. Oliver, et al., J. Appl. Phys. 109, 113106 (2011).
[69] A. Ciapponi, F. R. Wagner, S. Palmier and J.-Y. Natoli, J. Lumin. 129, 1786–1789 (2009).
[70] J.-Y. Natoli, L. Gallais, H. Akhouayri and C. Amra, Appl. Opt. 41, 3156–3166 (2002).
[71] L. Jensen, S. Schrameyer, M. Jupé, H. Blaschke and D. Ristau, Proc. SPIE 7504, 75041E-1 (2009).
[72] L. Gallais, J. Capoulade, J.-Y. Natoli and M. Commandré, J. Appl. Phys. 104, 053120 (2008).
[73] J. Dijon, T. Poiroux and C. Desrumaux, Proc. SPIE 2966, 315 (1997).
[74] J. Y. Natoli, L. Gallais, B. Bertussi, A. During, M. Commandré, et al., Opt. Express 11, 824–829 (2003).
[75] X. B. Cheng, H. F. Jiao, J. L. Lu, B. Ma and Z. S. Wang, Opt. Express 21, 14867–14875 (2013).
[76] S. Papernov and A. W. Schmid, Proc. SPIE 7132, 71321J-1 (2008).
[77] S. Papernov and A. W. Schmid, J. Appl. Phys. 82, 5422 (1997).
[78] M. D. Feit, L. W. Hrubesh, A. M. Rubenchik and J. N. Wong, Proc. SPIE 4347, 316 (2001).
[79] S. Papernov, E. Shin, T. Murray, A. W. Schmid and J. B. Oliver, Proc. SPIE 8530, 85301H-1 (2012).
[80] T. A. Laurence, J. D. Bude, N. Shen, T. Feldman, P. E. Miller, et al., Appl. Phys. Lett. 94, 151114 (2009).

Xinbin Cheng received his PhD in 2008 from the Tongji University. He is an Associate Professor of Optics at Tongji University. Since 2010, he heads the group 'High Power Laser Coatings' in the Institute of Precision Optical Engineering of Tongji University. His research interests comprise XUV multilayers, high power laser coatings, and nanometrological standards.

Zhanshan Wang received his PhD in 1996 from the Shanghai Institute of Optics and Fine Mechanics, Chinese Academy of Sciences. He is a Professor of Optics at Tongji University. He acts as the Director of the Institute of Precision Optical Engineering and an Executive Deputy Director of the Advanced Institute of Technology at Tongji University. He is mainly engaged in the research of the micro-imaging system in XUV to infrared range, and in the research of the design, fabrication, and characterization of multilayer optical elements in XUV to visible regions.